AGU PUBLICATIONS

Geochemistry, Geophysics, Geosystems

RESEARCH ARTICLE

10.1002/2017GC007258

Key Points:
- Sediment thicknesses and long-term sedimentation rates since 200 Ma are predicted
- Predictions are based on the age of the crust and the mean distance to the nearest passive margin
- Seafloor sediment-driven eustatic sea-level contribution has grown from 80 to 210 m since 120 Ma

Correspondence to:
A. Dutkiewicz,
adriana.dutkiewicz@sydney.edu.au

Citation:
Dutkiewicz, A., Müller, R. D., Wang, X., O'Callaghan, S., Cannon, J., & Wright, N. M. (2017). Predicting sediment thickness on vanished ocean crust since 200 Ma. *Geochemistry, Geophysics, Geosystems*, *18*, 4586–4603. https://doi.org/10.1002/2017GC007258

Received 27 SEP 2017
Accepted 28 NOV 2017
Accepted article online 8 DEC 2017
Published online 26 DEC 2017

© 2017. American Geophysical Union. All Rights Reserved.

Predicting Sediment Thickness on Vanished Ocean Crust Since 200 Ma

A. Dutkiewicz[1], R. D. Müller[1,2], X. Wang[3], S. O'Callaghan[3], J. Cannon[1], and N. M. Wright[1]

[1]EarthByte Group, School of Geosciences, University of Sydney, Sydney, NSW, Australia, [2]Sydney Informatics Hub, University of Sydney, Sydney, NSW, Australia, [3]Data61, CSIRO, Australian Technology Park, Eveleigh, NSW, Australia

Abstract Tracing sedimentation through time on existing and vanished seafloor is imperative for constraining long-term eustasy and for calculating volumes of subducted deep-sea sediments that contribute to global geochemical cycles. We present regression algorithms that incorporate the age of the ocean crust and the mean distance to the nearest passive margin to predict sediment thicknesses and long-term decompacted sedimentation rates since 200 Ma. The mean sediment thickness decreases from ~220 m at 200 Ma to a minimum of ~140 m at 130 Ma, reflecting the replacement of old Panthalassic ocean floor with young sediment-poor mid-ocean ridges, followed by an increase to ~365 m at present-day. This increase reflects the accumulation of sediments on ageing abyssal plains proximal to passive margins, coupled with a decrease in the mean distance of any parcel of ocean crust to the nearest passive margin by over 700 km, and a doubling of the total passive margin length at present-day. Mean long-term sedimentation rates increase from ~0.5 cm/ky at 160 Ma to over 0.8 cm/ky today, caused by enhanced terrigenous sediment influx along lengthened passive margins, superimposed by the onset of ocean-wide carbonate sedimentation. Our predictive algorithms, coupled to a plate tectonic model, provide a framework for constraining the seafloor sediment-driven eustatic sea-level component, which has grown from ~80 to 210 m since 120 Ma. This implies a long-term sea-level rise component of 130 m, partly counteracting the contemporaneous increase in ocean basin depth due to progressive crustal ageing.

1. Introduction

The global volume of seafloor sediments is an impressive 150 million km^3 (Olson et al., 2016). Sediment thickness exceeds 18 km in the Bay of Bengal and the Gulf of Mexico (Whittaker et al., 2013) due to continental drainage of large sediment sources but typically ranges between 400 m and 1.8 km over middle-aged (ca. 60–120 Ma) ocean crust (Olson et al., 2016) draped by slowly accumulating pelagic deposits. Sedimentation is the second most important mechanism controlling the volume of ocean basins after seafloor spreading, causing sea-level variations in the order of 60 m at a rate of 10 m/My (Miller et al., 2005). The ability to reconstruct the volume of sediment on subducted seafloor is critical not only for constraining long-term changes in eustatic sea level (Southam & Hay, 1977), but also for calculating global carbon budgets that include estimates of subducted carbon sequestered in pelagic sediments.

Sediment thickness varies nonuniformly with the age of the ocean crust, with mean sediment thickness in the Indian and Atlantic oceans being four times higher than in the Pacific Ocean (Conrad, 2013), a difference that largely reflects proximity to passive continental margins (Olson et al., 2016). This difference has been considered by separately analyzing different present-day ocean basins (Conrad, 2013; Olson et al., 2016), but this approach is unsuitable for predicting sediment thickness in ancient ocean basins due to the dynamic switching of plate margins. The conversion of plate margins from passive/transform (high sedimentation rates) to active (low sedimentation rates), and vice versa, is relatively common (Müller et al., 2016). To capture the time-dependence of sedimentation in entirely or partly vanished ocean basins on the proximity to switching plate boundaries, we predict sediment thicknesses and deep-sea sedimentation rates over the lifetime of a given parcel of oceanic crust. We use regression algorithms that are trained using the dependence of observed sediment thicknesses and long-term sedimentation rates on the age of underlying ocean crust and the mean distance to the nearest passive margin.

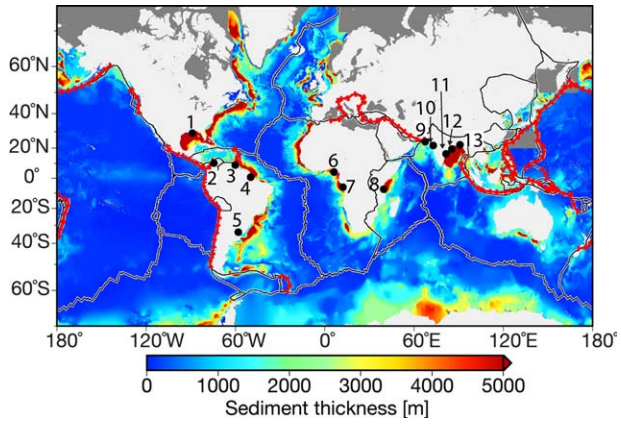

Figure 1. Minimum sediment thickness estimates based on global sediment thickness data set of Divins (2003) incorporating additions by Whittaker et al. (2013) and Wobbe et al. (2014) for the Southern Ocean. Plate boundaries indicated by black lines with white outlines and subduction boundaries indicated by red hatched lines. Mouths of major rivers (black circles) are: (1) Mississippi, (2) Magdalena, (3) Orinoco, (4) Amazon, (5) Paraná, (6) Niger, (7) Congo, (8) palaeo-Congo, (9) Indus, (10) Narmada, (11) Gondavari and Krishna, (12) Mahanadi, and (13) Ganges and Bramaputra (see Table 1). Gray denotes regions with no data. Mercator projection.

2. Data Sets and Methods

Our regression algorithms are based on a global sediment thickness grid of Divins (2003) with modifications by Whittaker et al. (2013) and Wobbe et al. (2014) for the Southern Ocean (Figure 1), based on a combination of published isopach maps, ocean drilling data, and seismic reflection profiles. Long-term mean sedimentation rates were calculated by decompacting global sediment thickness (Figure 1, see section 2.2) and using the present-day oceanic crustal age grid of Müller et al. (2016). Our analysis includes 12 rivers that globally discharge the largest detrital loads into ocean regions, and the paleo-Congo river (Figures 1 and 2, and Table 1).

We compute the distance of any given parcel of ocean floor to the nearest passive continental margin (defined as the boundary between continental and oceanic crust) at any given point during its lifetime using pyGPlates (www.gplates.org) at a grid resolution of 1°. The distances during the entire lifetime of a parcel of ocean crust at a given reconstruction time are used to find the mean distance for the relevant time interval. Each minimum distance, in that average, is the distance along the shortest path to all passive margins. Dijkstra's algorithm (Dijkstra, 1959; see supporting information Text S1) is used to find the shortest path to the closest passive margin segment. The algorithm does not allow the crossing of continents, subduction zones, or mid-ocean ridges. These restrictions are implemented given that passive margin sediments cannot cross continents, and generally do not cross subduction zones and mid-ocean ridges; there are some local examples of sediments bypassing plate boundaries (e.g., Carter et al., 2010; Rebesco et al., 2014) but this process is not common. Because our oceanic age grid reconstructions only go back to 230 Ma, we are not

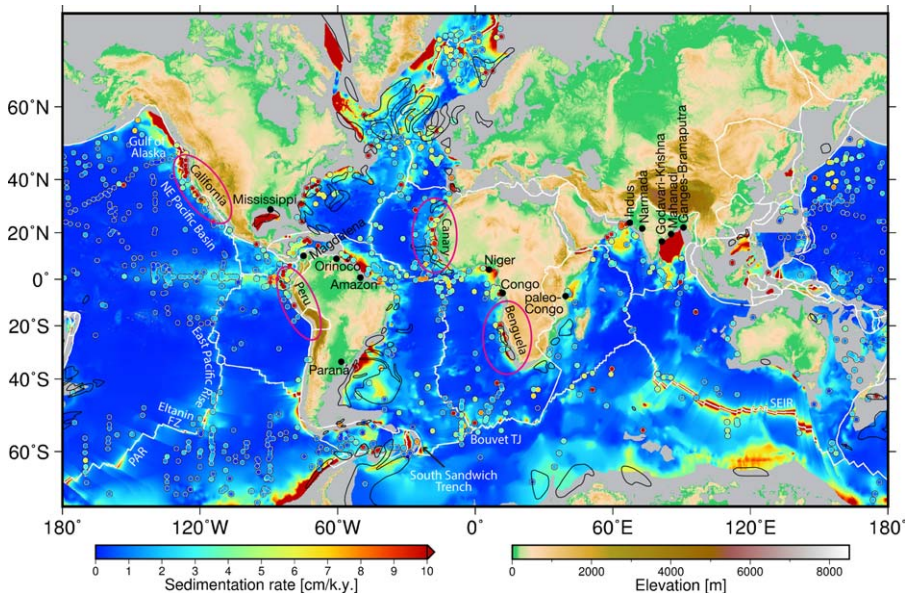

Figure 2. Decompacted long-term sedimentation rates overlain by short-term Quaternary sedimentation rates (colored circles—see data sets for details on data used). Black outlines are contourites from Rebesco et al. (2014), magenta outlines are major coastal upwelling zones from Capone and Hutchins (2013). Major rivers discharging into the ocean (Table 1) are based on a compilation by Milliman and Farnsworth (2011) and exclude rivers draining into regions where there is no sediment thickness data (gray areas). White lines indicate plate boundaries. Topography is based on the ETOPO1 global relief model (Amante & Eakins, 2009). Long-term sedimentation rates were calculated using the age grid of Müller et al. (2016) and the global sediment thickness grid of Divins (2003) incorporating additions by Whittaker et al. (2013) and Wobbe et al. (2014) for the Southern Ocean. Mercator projection.

Table 1
Top 12 Rivers Discharging into Ocean Regions of Known Sediment Thickness

River(s)	Lat. (°)	Lon. (°)	TSS (Mt/yr)	Max_elev (m)	Age range (Ma)	Age reference
Amazon	0.7	−50.1	1,200	5,500	24–0	Figueiredo et al. (2009)
Ganges-Bramaputra	22.1	90.8	1,060*	7,000	55–0	Curray (2014)
Mississippi	29.2	−89.3	400	3,700	35–0	Galloway et al. (2011)
Indus	24.0	67.4	250	7,800	50–0	Clift (2002)
Godavari-Krishna	16.3	81.4	234*	1,600	55–0	Curray (2014)
Orinoco	8.9	−60.5	150	6,000	25–0	Hoorn et al. (1995)
Magdalena	10.2	−74.9	140	3,300	14–0	Hoorn et al. (1995)
Paraná	−34.0	−58.4	90	>1,000	145–0	Potter (1997)
Narmada	21.7	72.8	70	1,100	50–0	Sant and Karanth (1993)
Mahanadi	19.4	85.4	61	440	55–0	Curray (2014)
Congo	−6.1	12.0	43	1,100	15–0	Stankiewicz and de Wit (2006)
Niger	4.2	6.0	40	820	80–0	Goudie (2005)
paleo-Congo	−7.4	39.4			100–55	Stankiewicz and de Wit (2006)

Note. Total suspended solids (TSS) are given as prediversion values from Milliman and Farnsworth (2011).
*—combined rivers. See Figures 1 and 2 for locations.

able to consider the full history of a parcel of ocean created before 230 Ma. However, for the vast majority of oceanic regions, this limitation has no effect. This is because Panthalassic ocean crust was always extremely distant from passive margins, as Panthalassa was entirely surrounded by subduction zones before ~83 Ma; equivalently, Atlantic and Tethyan ocean crusts were always proximal to passive margins. Even though the Tethys Ocean has undergone various phases of plate boundary switching throughout its lifetime, most of the Tethyan ocean floor in existence at 230 Ma was formed between two passive margins, namely that of northern Gondwanaland in the south and the southern margin of the Cimmerian terranes in the north (Matthews et al., 2016), representing a region that, like the Atlantic, was flanked by passive margins. In addition, the northern passive margin of the Cimmerian terranes flanked the northern portion of the Tethys, resulting in passive margin proximity for the remainder of the Tethys. Therefore, considering only part of their history still captures a representative snapshot of their mean distance to passive margins. Rare exceptions may be Tethyan regions where a switching of plate boundary types from active to passive or vice versa has occurred prior to 230 Ma. See supporting information Text S1 for additional details.

We compute grids of the distance to the mouths of the major rivers to assess their contribution to regions of anomalously high sedimentation rates along passive margins in the Cenozoic. For present-day, we use the distances within 1,500 km to these river mouths to simultaneously train our regressor for sediment thickness/sedimentation rate dependence on age, passive margin distance, and proximity to river mouths, enabling us to evaluate the contribution of these large rivers to the ocean's sedimentary budget. The well-established lasso regression method (Tibshirani, 1996) is applied to learn the relationship between the present-day crustal age, the present-day passive margin mean distance (Figure 3) and the present-day thicknesses/long-term sedimentation rates (Figures 1 and 2) as training data. Feature relationships were enriched by generating polynomial and interaction terms (Bishop, 2006), expressing the relationship between each of the interacting variables in terms of its effect on sedimentation. The robustness of the relationship was assessed using a cross-validation approach (Kohavi, 1995), where subsets of the training data were withheld during the learning procedure.

2.1. Data Sets

2.1.1. Short-Term Sedimentation Rates

A total of 1,291 short-term (Quaternary) sedimentation rates were compiled from various sources for comparison with long-term rates (Figure 2). Short-term sedimentation rates based on dated surface seafloor sediments were compiled from data sets of Broecker et al. (1991a, 1991b) and Seiter et al. (2005a, 2005b), Archer (unpublished; http://geosci.uchicago.edu/%7Earcher/server.html) incorporating core top data from Cwienk (1986), Lyle (2003, 2015), Chase et al. (2015), and Chase and Burckle (2015).

2.1.2. Major Rivers

Ages of the major rivers are based on a combination of fluvial and deep-sea fan sedimentary sequences, geo-chronology and thermo-chronology, and the timing of plate collisions. Paleo-Congo River is included,

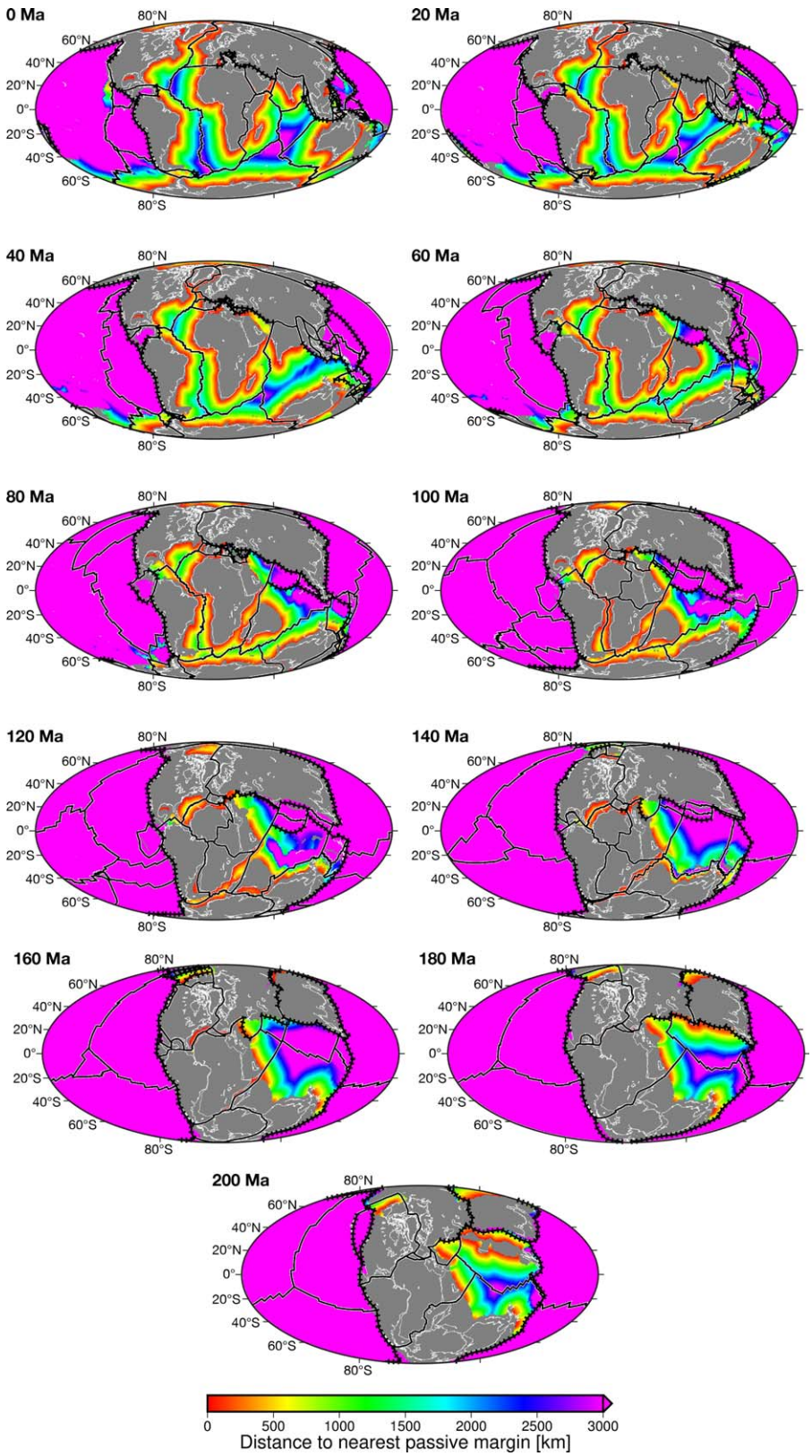

Figure 3. Mean distance to the nearest passive margin from 200 Ma to present-day at 20 my intervals, averaged for the lifetime of any parcel of ocean crust at a given reconstruction time. Black hatched lines denote subduction zones, and black lines with white outlines denote other plate boundaries. White outlines are paleo-coastlines and gray areas are continents. Mollweide projection.

which unlike the present-day Congo River discharged into the Indian Ocean (Stankiewicz & de Wit, 2006, Table 1).

All of these rivers originate in mountains (Milliman & Syvitski, 1992) with global discharge dominated by rivers associated with the Himalayan orogeny (Milliman & Farnsworth, 2011). Raymo (1994) suggests that river fluxes increased significantly following a major phase of deformation in the Himalaya orogen between ~21 and 17 Ma. This is considerably later than the inception of these rivers in the Eocene period (Table 1), further emphasizing the youthfulness of the currently observed river flux. Several major rivers (e.g., Huanghe, Changjiang, Colorado) were not included because they drain into oceanic areas where sediment thickness and hence long-term sedimentation rate are not known (see Figure 1).

The amount of global sediment discharge into the ocean is very difficult to calculate as potentially a significant proportion is deposited within rivers and associated deltas (Milliman & Farnsworth, 2011; Milliman & Syvitski, 1992). In addition, the present sediment flux of a given river may be very different from past fluxes (Milliman & Syvitski, 1992) as it depends on topography, drainage basin area, climate, precipitation, and lithology (Milliman & Farnsworth, 2011). In general, however, fluvial discharge is confined to the coastal zone (Milliman & Farnsworth, 2011) and covers a very small area compared to pelagic deep-sea sediments (Hay et al., 1988a). The largest rivers discharge into the ocean along passive margins (Figure 2) where the sediment accumulates in estuaries and the inner to middle continental shelf and may only be transported into the deeper ocean during falling sea-level and delta progradation (Milliman & Farnsworth, 2011). Smaller mountainous rivers that drain active continental margins discharge directly onto shelves and may by-pass the continental shelf during flooding or sea-level high stands (Milliman & Farnsworth, 2011; Milliman & Syvitski, 1992). We are unable to include the sediment contribution from 1,000+ small rivers as the sediment discharge into the ocean for the majority of these rivers and their ages of inception are not known (Milliman & Farnsworth, 2011). However, any contribution of these rivers into the deeper ocean, for example, as hyperpycnal flows, is encapsulated in the global sediment thickness grid of Divins (2003) in terms of the observed overall increase in sediment thickness toward continental margins (Figure 2).

2.2. Decompaction of the Total Sediment Thickness

For decompaction of the total sediment thickness required for calculating decompacted long-term sedimentation rates, we evaluated the exponential porosity-depth relationships from Bahr et al. (2001) established for sand, silt, and shale lithologies in deep-sea sedimentary columns. We integrated the porosity-depth relationship for shale given in equation (1) because it is the most representative lithology for the deep-sea sediment column as its porosity change with depth is similar to that of the equally ubiquitous calcareous oozes (Hamilton, 1976):

The following decompaction equation is derived from Bahr et al. (2001) based on their porosity-depth relationship for shale:

$$Z_d = \frac{Z_t + \left[\left(\frac{\phi_0}{c}\right) \times (\exp(-c \times Z_t) - 1)\right]}{1 - \phi_0} \tag{1}$$

where Z_d is the decompacted sediment thickness, Z_t is the total observed compacted sediment thickness, ϕ is the porosity, and c is an empirical constant that depends on a variety of underlying processes that affect the compaction of sediment (see Bahr et al., 2001).

2.3. Algorithm Input Data

We use three types of input data: sediment thickness (ST) (Figure 1) or long-term sedimentation rate (SR) (Figure 2), age of oceanic lithosphere (Müller et al., 2016), and the mean distance of a given location on ocean crust to the nearest passive margin (Figure 3). All grids are downsampled to 1° × 1° degrees to facilitate computationally efficient machine leaning and considering that sediment thickness and sedimentation rates change gradually as a function of location. We take the logarithm of both sediment thickness and sedimentation rates for training our regression model because of the large dynamic range of both parameters. Large portions of the abyssal ocean floor have relatively little sediment and very slow sedimentation rates, whereas the converse holds for regions close to passive continental margins. If we were to train our model on unscaled input data, our machine learning algorithm would incorrectly focus its attention primarily on the regions of thickest sediment or highest sedimentation rates at the detriment of the low ends of our

input value ranges. This is because a 5% error of a large number is significantly greater than a 5% error of a small number. By modeling the log(ST) and log(SR), this effect is substantially reduced.

2.4. Algorithm Design

2.4.1. Lasso Regression Model

Lasso, also known as the *least absolute shrinkage and selection operation*, is a regression model that tries to find the best parameters that model the relationship between the input features and target data by maximizing a cost function. To reduce model overfitting, L1-regularization (a penalty on large parameter values) was employed. Compared with L2-regularization, L1 regularization tends to produce many coefficients with zero values or very small values and only a few coefficients with large values, which is more robust for outliers. Basically, given a set of samples, $X=[\boldsymbol{x}_1, \boldsymbol{x}_2, \ldots, \boldsymbol{x}_N]$, where each sample is a vector $x_i \in R^d$ $(i=1,2,\ldots,N)$ and is associated with a target variable $y_i \in R$. Lasso tries to find the best coefficients $\boldsymbol{w} \in R^d$ so that the objective cost function is minimized, i.e., Lasso tries to find $\boldsymbol{w}^*$

$$\boldsymbol{w}^* = argmin \sum_{i=1}^{N}\left(y_i - \sum_{k=1}^{d} x_{ik} w_k\right)^2 + \alpha \sum_{j=1}^{d} |w_i| \tag{2}$$

where α is the regularization parameter and $\alpha \sum_{j=1}^{d} |w_i|$ is the L1 term. The optimal relationship is generated when $\alpha=0.01$.

2.4.2. Polynomial Feature Generation

Polynomial feature generation is a technique that generates a new feature matrix consisting of all polynomial combinations of features with a degree less than or equal to the specified degree. For example, if there are only two features in the original sample, then the degree-2 polynomial features are: 1, age of ocean crust (A), distance to passive margin (D), A^2, AD, and D^2. Degree-3 polynomial features were generated to train the model based on feature age, distance to margins, and distance to major rivers. Polynomial feature generation is used to enrich the feature space and prompt the model to identify potential complex relationships between the features and the target variable.

2.4.3. Longitude k-Fold Cross-Validation

Cross-validation, a model validation technique, avoids overfitting and derives a more accurate estimate of model prediction performance. In k-fold cross-validation (Kohavi, 1995), the original samples are partitioned longitudinally into k equal sized subsamples. Among the k subsamples, a single subsample is retained as the validation set for testing model, and the remaining $k-1$ subsamples are used to train the model. The cross-validation process is repeated k times with each of the k subsamples used exactly once as the validation data.

Our original random k-fold cross-validation caused a problem that the sedimentation rate is mainly predicted by longitude and latitude, instead of the features of interest to us. To resolve this issue, we designed a new partition algorithm that partitions samples based on their longitude so that the validation set is spatially distant from training set. This technique successfully eliminated the effect of longitude and latitude and encouraged the model to learn the relationship between features of our interest and the target variable.

2.4.4. Integration of the "Distance to Major River Mouths"

The distance of each sample to the major river mouths was calculated using a python script. The influence of each river on the sediment rate was set as a free parameter and learnt during the training phase using the COBYLA (Powell, 1978) optimization algorithm. COBYLA, also known as *constrained optimization by linear approximation*, is a numerical optimization method for constrained problems where the derivatives of the object function are not known.

2.4.5. The Influence of Rivers on Sedimentation Rate

We have trained two regression models in order to better understand the effect of distance to major rivers on sedimentation rate. One model learns the dependence of sedimentation rate and sediment thickness on age and distance to margins and using sediment samples outside of a prespecified distance from major river mouths. The other model learns the dependence of sedimentation rate and sediment thickness on age, distance to margins, and distance to major rivers using all available samples. At each geological reconstruction time from 200 to 0 Ma, we predict sedimentation rate and sediment thickness by querying a given regression model using relevant features.

2.4.6. Standardization of Parameters

We use feature scaling to standardize the range of our independent variables and thus remove the influence of the unit of measurement of predictor and outcome variables. Our standardization is based on the following equations and parameters:

$$A' = \frac{A - \mu_A}{\sigma_A} \tag{3}$$

where A' is the standardized age of the ocean crust, A is the age of the ocean crust, μ_A is the mean age of the ocean crust (60.2 my), and σ_A is the standard deviation of age (43.5 my), and

$$D' = \frac{D - \mu_D}{\sigma_D} \tag{4}$$

where D' is the standardized distance from a passive margin, D is the distance from passive margins, μ_D is the mean distance to passive margins (1878.2 km), and σ_D is the standard deviation of distance from passive margins (1076.8 km). The age and mean distance to nearest passive margin are limited to 200 Ma and 3,000 km for the purpose of paleo-thickness and paleo-sedimentation rate predictions—see supporting information Text S1 and Figure S1 for additional details.

3. Predictive Models of Sediment Thickness and Sedimentation Rate

Our regression algorithms yield the following predictive relationships (Figure 4), considering sediments outside a 1,500 km distance from major river mouths:

$$logST_{compacted} = 5.37 + 0.44A' - 0.15D' - 0.24A'^2 - 0.06A'D' + 0.01D'^2 + 0.07A'^3 - 0.33D'^3 \tag{5}$$

and

$$logSR_{decompacted} = -1.01 - 0.31A' - 0.20D' + 0.39A'^2 - 0.13A'D' - 0.11A'^3 - 0.03A'^2D' - 0.02A'D'^2 - 0.37D'^3 \tag{6}$$

where ST is the sediment thickness in meters, SR (cm/ ky) is the sedimentation rate, A' is the standardized age of the ocean crust, and D' is the standardized distance from a passive margin (see section 2.4.6). The associated regression surfaces show a distinct change in gradient that discriminates two distinct regions at a mean distance to the nearest passive margin of ~2,000 km (Figure 3). Region A includes all oceanic

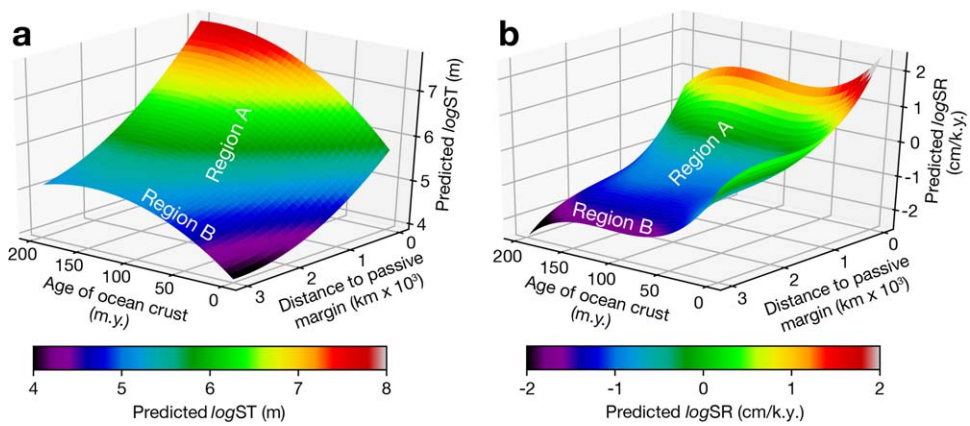

Figure 4. Regression surfaces (equations (5) and (6)) showing the relationship between age of ocean crust, mean distance to the nearest passive margin of a given parcel of ocean crust since its formation and (a) predicted (compacted) sediment thickness (ST) and (b) long-term sedimentation rate from decompacted sediment thickness (SR). Region A reflects areas close to passive continental margins, while region B represents areas that are not influenced by terrigenous sediments from passive margins. In our application of these two models to reconstructed ocean basins, all ocean floor with mean distances larger than 3,000 km to the nearest passive margin throughout its lifetime is represented by distances of 3,000 km, as terrigenous sediment originating from passive margins only affects oceanic sedimentation up to distances of ~3,000 km (see supporting information).

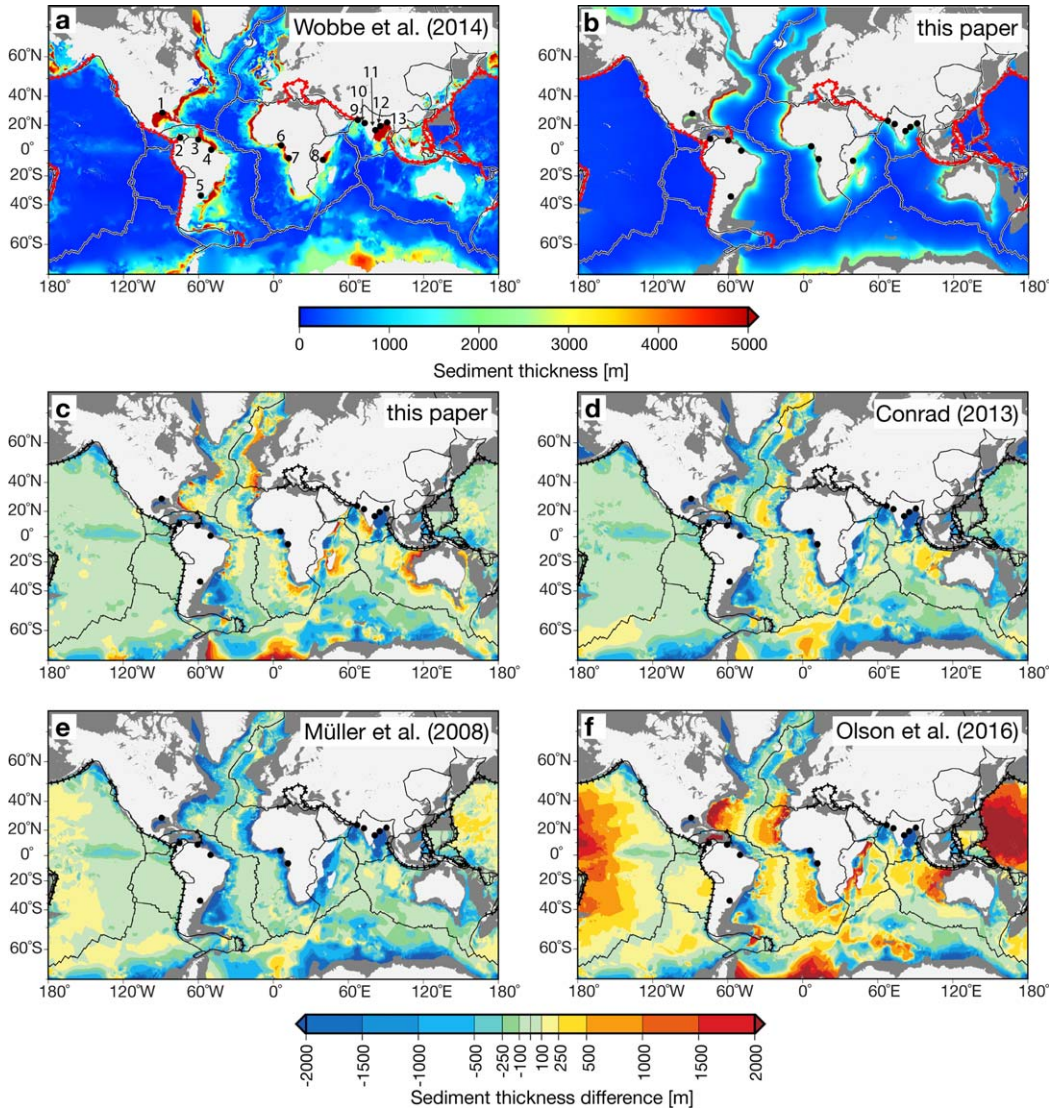

Figure 5. Computed differences between observed (a) and predicted global ocean sediment thicknesses based on (c) the oceanic crustal age-mean distance to nearest passive margin regression algorithm presented in this paper (without the influence of major rivers) (b), (d) the oceanic crustal age relationships determined for the Pacific, Atlantic, and Indian ocean basins of Conrad (2013) that also consider a latitude dependence, (e) the simplified relationship of sediment thickness as a function of oceanic crustal age and latitude from Müller et al. (2008), and (f) global best-fit polynomial relationship of Olson et al. (2016). All calculations were made using the updated oceanic age grid of Müller et al. (2016). Plate boundaries indicated by black lines with white outlines and subduction boundaries indicated by red hatched lines in Figures 5a and 5b. Plate and subduction boundaries are indicated by black lines and black hatched lines, respectively in Figures 5c–5f. Mouths of major rivers (black circles) as in Figure 2. Gray denotes regions with no data. Positive values indicate overestimated sediment thicknesses. The mean misfit for our model (c) is 137 m (median = −4 m), with the well-fit regions shown in light green comprising ~75% of the seafloor. The mean misfit of the other models is: (d) 266 m (median = 39 m), (e) 285 m (median = 10 m), and (f) −323 m (median = −174 m). Mouths of major rivers (black circles) are: (1) Mississippi, (2) Magdalena, (3) Orinoco, (4) Amazon, (5) Paraná, (6) Niger, (7) Congo, (8) palaeo-Congo, (9) Indus, (10) Narmada, (11) Gondavari and Krishna, (12) Mahanadi, and (13) Ganges and Bramaputra (see Table 1). Mercator projection.

regions proximal to passive margins, with the greatest sediment thicknesses and sedimentation rates, irrespective of the age of ocean crust, occurring in the North Atlantic Ocean and Southern Ocean south-east of Australia. These regions have been in relative proximity (>2,000 km) to passive margins throughout their lifetime (Figure 3). Region B is dominated by areas where extremely low sedimentation rates (<0.1 cm/ky) prevail, associated with a thin sediment cover (<100 m), reflecting large distances of at least ~3,000 km to the nearest passive margin (Figures 3 and 4b). These areas, which are constrained to the Pacific Ocean

today, but included substantial portions of the Tethys Ocean in the past (Figure 3), receive little terrigenous input (Rea, 1994).

Our prediction for sediment thickness and sedimentation rate which includes the contribution of rivers yields a regression parameter array. The array incorporates optimal weights of the distance to each river mouth and includes a set of third-order polynomial coefficients for fitting sediment thickness and sedimentation rates as a function of crustal age, distance to passive margins, and distance to major river mouths (see supporting information). We use the regression analysis including rivers merely to discern what contribution relatively recently formed rivers may have made to deep-sea sedimentation. We cannot use this algorithm for predicting deep-sea sedimentation for the bulk of our model time, as nearly all currently existing major rivers did not exist for at least 75% of our model time period.

We compare our model for sediment thickness prediction without considering rivers with three alternative models. These include a regionalized model akin to that proposed by Conrad (2013), as well as the model by Müller et al. (2008), as applied to the updated oceanic age grid by Müller et al. (2016) (see supporting information Figure S2 for details), and the global cubic polynomial relationship by Olson et al. (2016). In addition, we compare our predicted sedimentation rates with the global cubic polynomial relationship between sedimentation rates and age proposed by Olson et al. (2016). Computed differences between all predicted sediment thicknesses for the present are compared with present-day observations (Wobbe et al., 2014) (Figure 5). The difference grids reveal that of all predictive relationships, ours most closely matches the present-day thickness with a moderate mean underestimation of 137 m (median = −4 m). The Conrad (2013) and Müller et al. (2008) relationships show a substantially larger underestimation with means of 266 m (median = 39 m) and 285 m (median = 10 m), respectively, while the Olson et al. (2016) global polynomial relationship shows a very large overestimation with a mean of −323 m (median = −174 m). We have included sediment thickness maps from 0 to 200 Ma in 20 my intervals for all models in supporting information (Figures S3–S5, see supporting information Figure S6 for mean sediment thicknesses through time), as well as for the predicted sedimentation rate grids based on Olson et al.'s model (supporting information Figure S8). Sediment thickness predictions based on Olson et al.'s (2016) global method (supporting information Figure S7) result in a substantial overestimation (Figure 10b) of sedimentation rates while their method for estimating sedimentation rates (supporting information Figure S7) results in an underestimate (Figure 10c). This underestimate arises because of these models' inability to predict elevated sedimentation rates proximal to passive margins because the Olson et al. (2016) polynomial models are constrained only by sediments on ocean floor aged 0–120 my. The same age limitation results in an overestimate of sediment thickness on old ocean crust due to the extrapolation of their polynomial relationship for ages older than 120 Ma. Olson et al. (2016) also present a large set of polynomial relationships regionalized for today's ocean basin physiography, which result in better fits for individual regions. This is also the case for the regionalized approach we adopt for following the model proposed by Conrad (2013). However, such an approach is not useful for predicting sediment thickness in reconstructed, now vanished ocean basins, as it is not straightforward to determine how they may correspond to today's ocean basins. For instance, parts of the Tethys Ocean resembled today's Pacific Ocean in being very distal to passive margins, whereas the opposite holds for other parts of the Tethys, and the relative portions of the Tethys that were "Pacific-like" versus "Atlantic-like" have changed through time (see Figure 4). This is what motivates us to develop an algorithm that detects the tectonic, and thus sedimentary, setting of different ocean basins automatically.

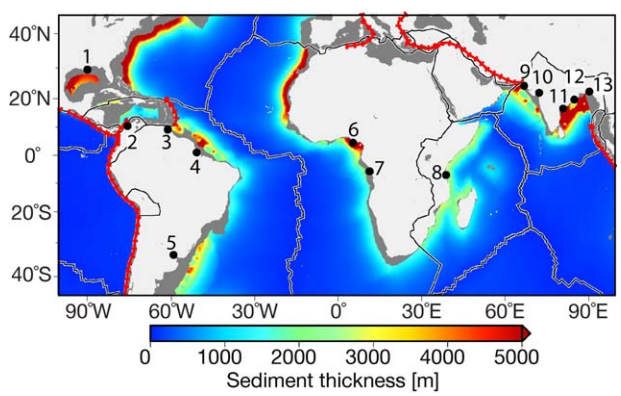

Figure 6. Predicted sediment thickness that includes the contribution of rivers within a 1,500 km distance to the nearest river mouth. Mouths of major rivers (black circles) are: (1) Mississippi River, (2) Magdalena River, (3) Orinoco River, (4) Amazon River, (5) Paraná River, (6) Niger River, (7) Congo River, (8) palaeo-Congo River, (9) Indus River, (10) Narmada River, (11) Gondavari and Krishna rivers, (12) Mahanadi River, and (13) Ganges and Bramaputra rivers (Table 1). Mercator projection.

We find that the contribution of rivers (Figure 6 and Table 1) is localized to within a radius of 1,500 km from their mouths, with the exception of the Bengal Fan which is twice as large (Curray, 2014). Including the effect of major rivers adds the equivalent of a 31 m thick layer of sediment globally. We exclude the contribution of rivers from our model (Figure 5b) to avoid biasing our predictions on ocean crust proximal to passive continental margins by such localized young

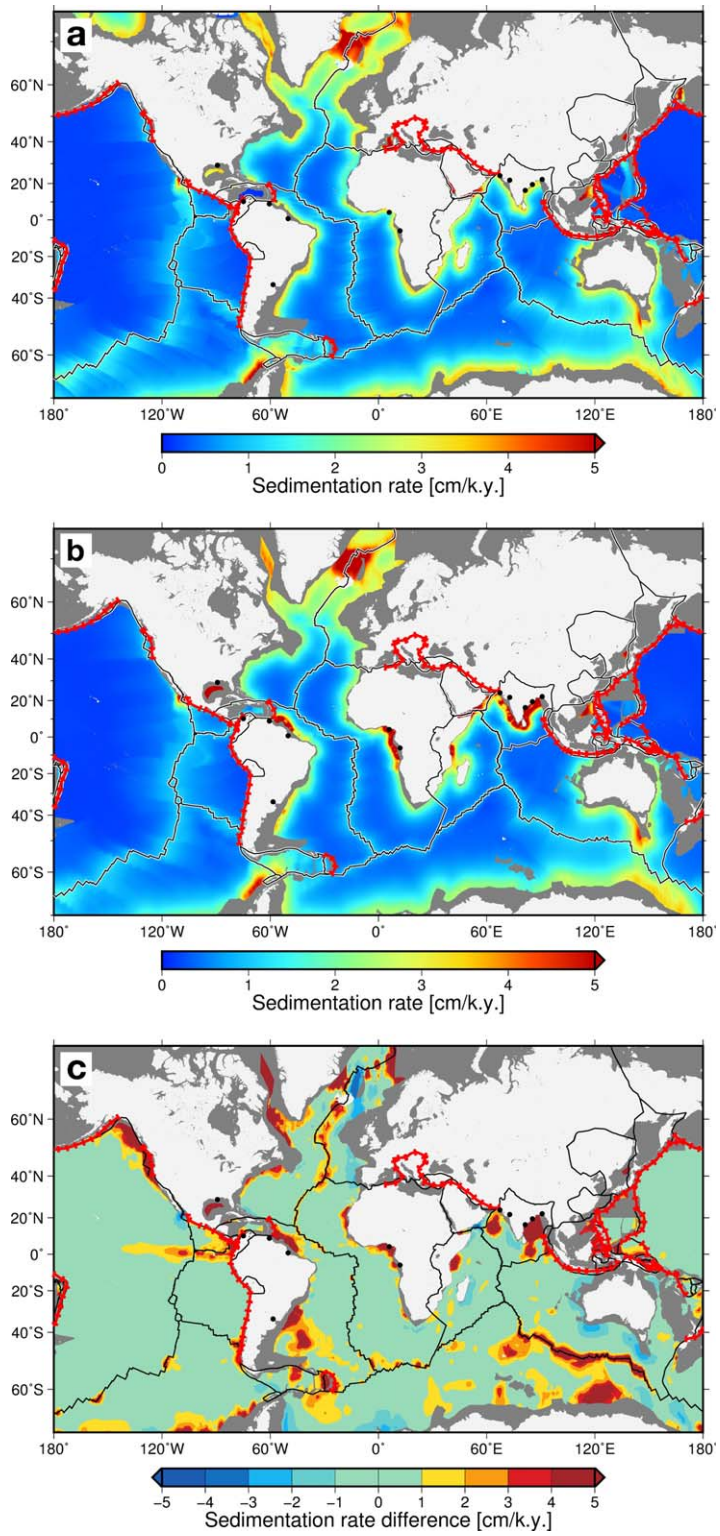

Figure 7. Predicted global ocean sedimentation rates. Plate and subduction boundaries are indicated by black lines (with white outlines in Figures 7a–7c) and red hatched lines, respectively. Mouths of major rivers (black circles) as in Figure 1. Gray denotes regions with no data. (a) Predicted sedimentation rates that exclude contributions from major rivers. (b) Predicted sedimentation rates that include the contribution of rivers within a 1,500 km distance to the nearest river mouth. (c) Difference in sedimentation rates between observed long-term sedimentation rates (Figure 2) and predicted sedimentation rates without rivers (b). Mercator projection.

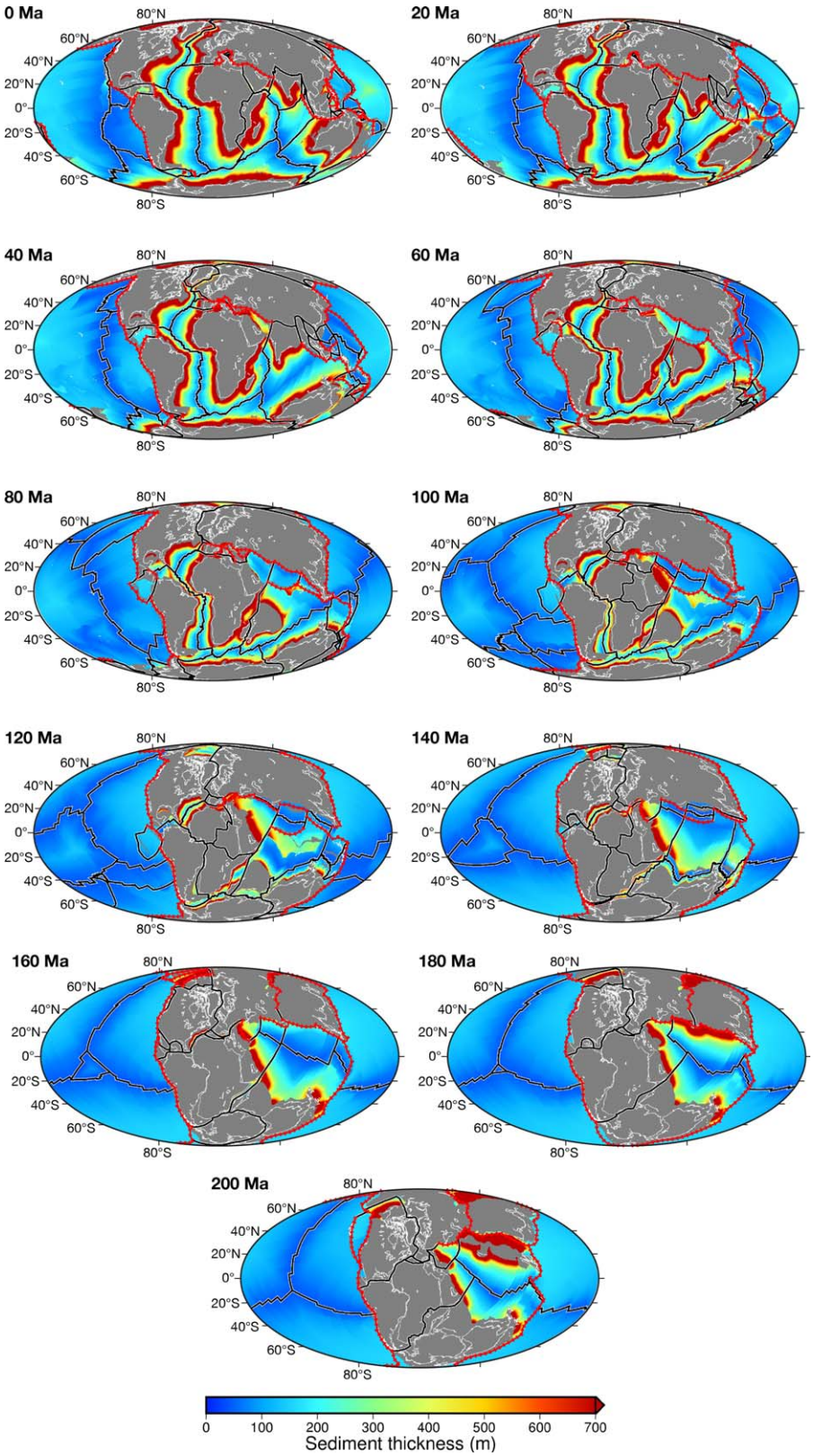

Figure 8. Predicted sediment thicknesses from 200 Ma to present-day at 20 my intervals. Line notations as in Figure 1. White outlines are paleo-coastlines. Gray indicates continental regions. Mollweide projection.

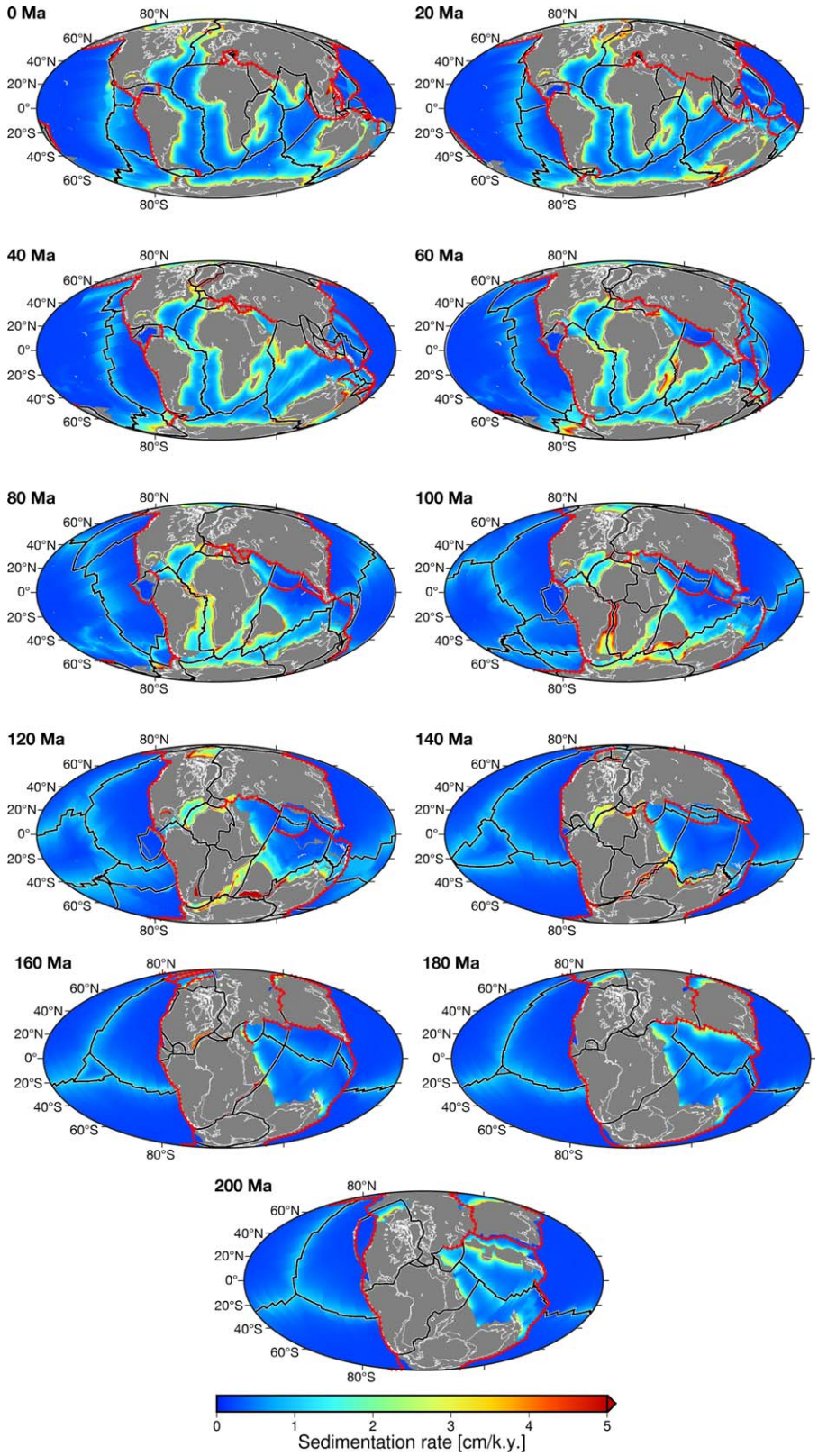

Figure 9. Predicted long-term sedimentation rates from 200 Ma to present-day at 20 my intervals. Line notations as in Figure 1. White outlines are paleo-coastlines. Gray indicates continental regions. Mollweide projection.

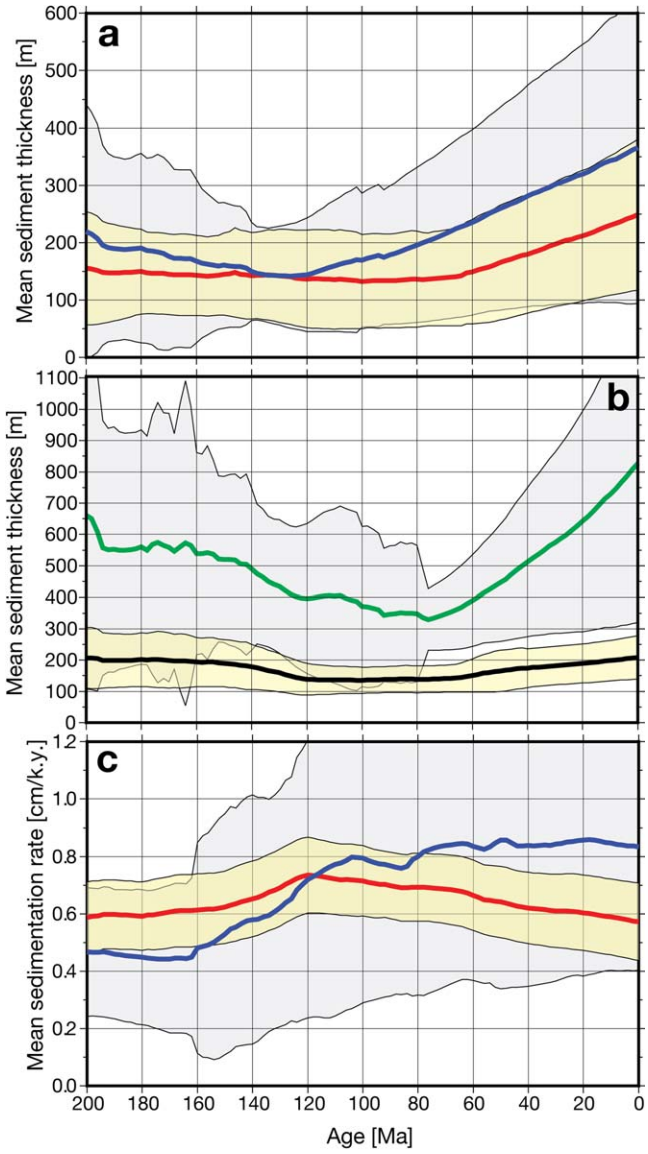

Figure 10. Variations in sedimentation (mean and standard deviation) through time at 2 Ma intervals. Shaded regions indicate standard deviation. (a) Blue line denotes predicted sediment thickness that considers the mean distance to the nearest passive margin and age of ocean crust described by equation (3) and Figure 7a. Red line denotes predicted sediment thickness based on three regionalized relationships following Conrad (2013) with an additional consideration of the latitude dependence of sedimentation in these regions. (b) Green line represents sediment thickness prediction based on Olson et al. (2016) global cubic polynomial sediment thickness-age relationship and black line that of Müller et al.'s (2008) method applied to the revised set of paleo-oceanic age grids (Müller et al., 2016). The former model strongly overestimates global sediment thickness because Olson et al.'s (2016) model is only constrained by sediments on floor younger than 120 Ma, while the latter underestimates sediment thickness as distance to passive margins is not taken into account. (c) Predicted sedimentation rate based on equation (4) and Figure 7b (blue) versus sedimentation rates from Olson et al.'s (2016) global cubic rate-age relationship.

anomalies (see Table 1), considering that for most parts of Earth history large, high uplifts associated with very large rivers were absent (Hay et al., 1988b). This is consistent with an increase in the length of collision plate boundaries from about 2,500 to 28,500 km between 55 and 40 Ma (Rona & Richardson, 1978). The median difference between the observed (Figure 5a) and modeled present-day sediment thickness that excludes rivers (Figure 5b) is 4 m, and the equivalent median difference in sedimentation rates is 0.005 cm/ky (Figure 5c). We cannot predict the time-dependent growth of river contributions to sedimentation in our model because the total sediment thickness alone does not provide sufficient information to model these processes, which are tied to the uncertain uplift and erosion history of individual mountain chains and continental interiors. As a consequence, we restrict ourselves to excluding regions in the proximity of major river mouths to avoid biasing the bulk of our model history when both highly elevated orogens and associated rivers were rare.

We do not compute sedimentation rates (SR) from the time derivative of sediment thickness (ST) because sedimentation rates need to be computed based on decompacted sediment thickness—otherwise SR will be underestimated, as progressive compaction of sediments with depth reduces the apparent sedimentation rate. Therefore, accurate sedimentation rates cannot be obtained from differences in our computed total long-term, compacted sediment thicknesses through time. Instead, we compute long-term sedimentation rates from decompacted sediment thickness and compare them to short-term sedimentation rates, as they are both based on decompacted sediments (Figures 2 and 7). In other words, SR estimates from the time derivative of ST will always be substantially smaller than those from decompacted sedimentation rates. Long-term sedimentation rates (Figure 7) are in a good agreement with short-term rates (Figure 2), except for regions of unusually high values (>10 cm/ky) near continental margins associated with major rivers, upwelling zones and geologically young glacial deposits at mid-latitude to high latitude (Hay et al., 1988a). Instances of anomalous modern sedimentation rates are also linked to redistribution of sediments by bottom currents (Figures 1b and 2) (e.g., Rebesco et al., 2014) and exceptionally low sedimentation rates (Rea et al., 2006).

Sedimentation rates are higher along mid-ocean ridge crests and young flanks aged 0–40 my as compared with older mid-ocean ridge flanks (Figure 7a). This is because mid-ocean ridges are elevated above the carbonate compensation depth (CCD), which has had an average global depth of 4.2 km over the last 50 Ma (Boss & Wilkinson, 1991), and thus accumulate biogenic carbonate, in contrast to ridge flank portions below the CCD. Mean long-term sedimentation rates increase substantially as ocean crust ages because of the large proportion of old crust proximal to passive margins including much of the Atlantic and Indian oceans as well as the South Pacific (Figure 3), which supply terrigenous material into the ocean, or have experienced relatively high biosiliceous productivity (Robinson et al., 2004).

4. Tectonic Controls on Sedimentation

The application of our predictive algorithm using grids of crustal reconstructions and mean distances to passive margins through time (Figure 3) produces 201 oceanic paleo-sediment thickness and paleo-

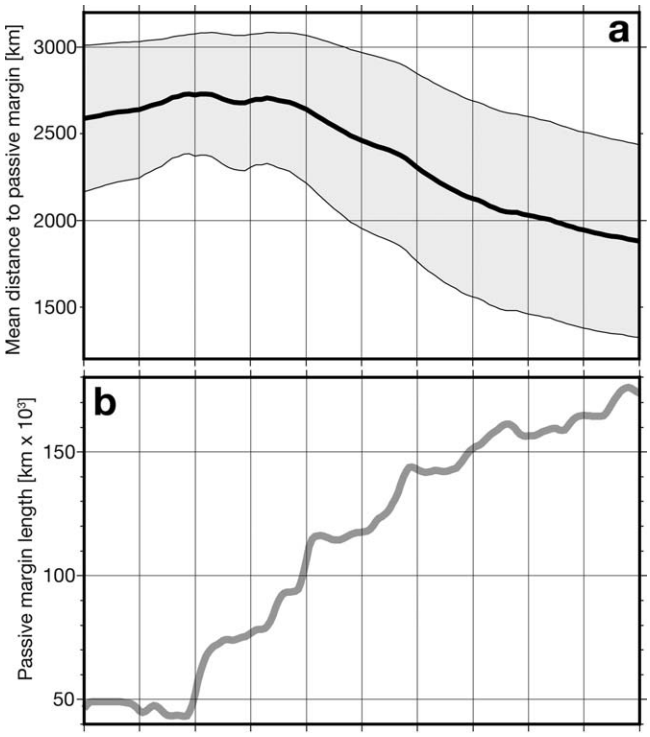

Figure 11. (a) Mean distance of individual parcels of ocean floor to nearest passive margin throughout their lifetime. This distance was at a maximum before 140 Ma, when many current ocean basins had not yet formed and the bulk of existing ocean floor was relatively distal to passive margins. Shaded regions indicate standard deviation. (b) Length of passive margins along emerged continental crust through time; more than tripling during the main phase of Pangea breakup and dispersal postdating 160 Ma.

sedimentation rate grids from 200 Ma to the present (Müller et al., 2016) (Figures 8 and 9). These maps reveal several regions with anomalously large sediment thicknesses in proximity to subduction zones that reflect the switching of a passive to an active margin, or conversely anomalously small sediment thicknesses along margins that switched from an active to a passive margin. Examples of such anomalies include the Vardar Ocean (western Tethys; passive to subduction, 170 Ma) the margins of west Antarctica (southern Pacific; subduction to passive, ~85 Ma), Arabia (subduction to passive, ~75 Ma), north India (Neo-Tethys Ocean; passive margin to subduction zone, ~60 Ma), and western North America (subduction to transform, ~30 Ma) (Müller et al., 2016). In addition, rifting of ribbon terranes away from passive margins, results in old and sediment-rich ocean crust crossing an ocean basin toward a subduction zone (e.g., the separation of Argoland and associated terrains from the northern margin of Gondwanaland (Gibbons et al., 2015)), also resulting in a sediment thickness anomaly in proximity to a subduction zone. These examples highlight the importance of capturing the dynamic nature of ocean basin margins through time for predicting long-term sediment thickness or sedimentation rates.

Paleo-sediment thicknesses are likely to be slightly overestimated prior to the Tithonian (150 Ma), marking the first significant occurrence of calcareous pelagic sediment in the deep-sea record (Bornemann et al., 2003). Sedimentation rates in the Late Berriasian reached values similar to those of modern deep-sea calcareous oozes that are also dominated by coccolithophorids (Bornemann et al., 2003). The deposition of significant volumes of pelagic carbonate occurred from ~150 Ma when the CCD increased by almost 1.5 km below the average depth of mid-ocean ridge crests (Boss & Wilkinson, 1991), allowing carbonate to be preserved on a substantially greater area of the seafloor similar to present-day. Prior to 150 Ma deep-sea sedimentation was dominated by slowly accumulating pelagic clays derived from desert dust that accumulated as residual sediment below the CCD (Berger & Winterer, 1974) that was relatively shallow (Boss & Wilkinson, 1991).

Sediment thickness and sedimentation rates increase with decreasing age (Figure 10) and are coupled to a decrease in mean distance to the nearest passive margin (Figure 11a) and an increase in the length of passive margins (Figure 11b). Sediment thickness ranges between ~150 and 210 m from 200 to 120 Ma, reflecting a shortage of passive margins during this period and the presence of vast subduction zones that are efficient sediment traps. After 120 Ma, sediment thickness climbs steadily toward a present-day value of ~365 m (Figure 10a). This increase is due to the ageing ocean crust proximal to post-Pangea passive margins being subject to prolonged sedimentation since opening of the ocean basins (Figure 8). Global long-term sedimentation rates are near constant at ~0.45 cm/ky. between 200 and 160 Ma, increasing to ~0.8 cm/ky between 160 and 100 Ma due to the formation of young mid-ocean ridge flanks close to passive margins (Figure 9). The mean distance to the nearest passive margin begins to gradually decrease after 140 Ma (Figure 11a) and the total length of passive margins increases from $\sim 40 \times 10^3$ to $\sim 65 \times 10^3$ km from 160 to 140 Ma (Figure 11b).

Our Cenozoic predicted sediment thickness (Figure 10a) is significantly larger than that based on a regionalized age-latitude relationship, because our method considers the growing influence of passive margins on total sediment thickness on old ocean floor in the Atlantic and Indian oceans. Our modeled rates capture a wide range of oceanic sedimentation rates in different tectonic settings, resulting in a large standard deviation, and a substantial increase in rates from 160 to 100 Ma, reflecting the growth of passive margins during this period (Figure 9), while Olson et al.'s (2016) rates reflect a pure age relationship, and are thus much more constant through time. For comparative purposes, supporting information Figure S7 shows all four models shown in (a) and (b) on one figure, albeit without standard deviations.

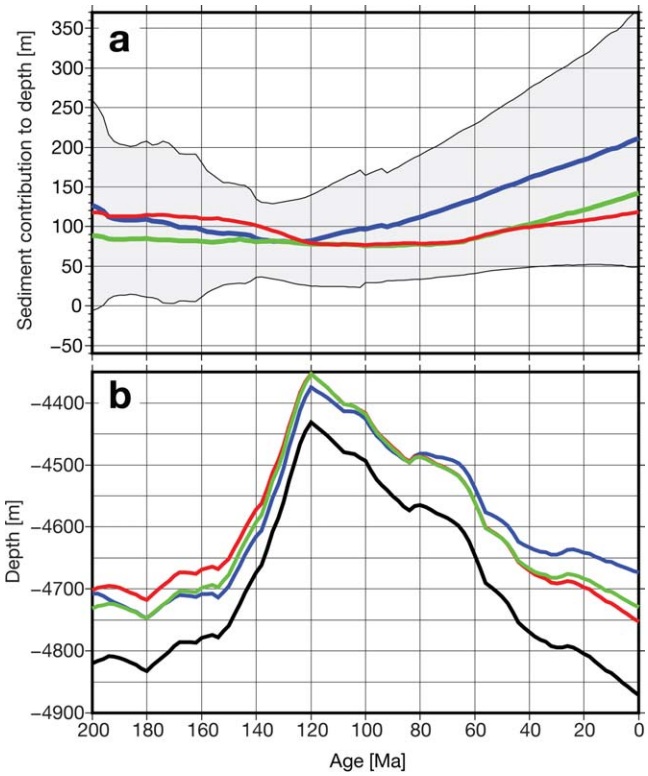

Figure 12. (a) Contribution of sediment thickness change to depth. The blue curve shows our best estimate of the contribution of ocean sediments to depth, considering isostatic compensation of sediments; shaded region indicates standard deviation. The red curve illustrates the equivalent model based on a simplified relationship of sediment thickness as a function of oceanic crustal age and latitude from Müller et al. (2008), applied to the oceanic paleo-age grids of Müller et al. (2016), while the green curve shows a model based on a regional age-latitude relationship (supporting information Figure S2), separating the Pacific, Atlantic, and Indian oceans, similar to the approach by Conrad (2013). (b) The black curve outlines the evolution of mean oceanic basement depth from applying the GDH-1 age-depth relationship of Stein and Stein (1992) to the paleo-age grids from Müller et al. (2016), while the blue, red, and green colored curves show the combined effect of oceanic basement depth change (black) and the effect of isostatically compensated sediment thickness from the models as in Figure 12a.

5. Implications for Eustasy and Unmapped Regions

Our predictive algorithms based on the age of ocean crust and distance to nearest passive margin allow us to trace the history of sedimentation in the global ocean, including its accumulation and destruction on now vanished ocean crust, in a plate tectonic context. It also allows us to assess the impact of sediment thickness in paleo-ocean basins including now subducted ocean crust, on the first order sea-level fluctuations based on ocean volume.

We calculate that sea level would be ~210 m lower than it is today (Figure 12a) without the volumetric contribution of sediments following an application of the isostatic compensation method by Sykes (1996). This method established a model for relating total sediment thickness to the associated isostatic correction using density-depth equations for deep-sea sediments. This is 20% different from the 166 m estimate obtained by Conrad (2013). Our own, modified implementation of Conrad's (2013) approach (Figure 12a) results in a similar value close to 150 m. Our estimated contribution of sediments to sea level was at its lowest (~80 m) between 140 and 120 Ma. During this period, Panthalassa (Figures 9 and 10) dominated contributions to global sediment thickness. The giant Panthalassa ocean was enveloped by subduction zones and was largely far removed from sources of terrigenous material.

Müller et al. (2008) suggested that global sea level fell by ~110 m after 80 Ma based on the combined effects of decreasing mid-ocean ridge volume, emplacement of oceanic plateaus and increasing sediment accumulation. Their calculation included an estimated increase in the sediment thickness contribution to sea level of 60 m since 80 Ma, implying that sea level would have fallen by ~170 m without any seafloor sedimentation. Here we increase the estimate in the sedimentary contribution since 80 Ma to 100 m, revising the total subsequent sea level fall from 110 to 70 m (not including glacio-eustatic contributions). This emphasizes the importance of sediment thickness estimates for modeling long-term eustasy.

Our sediment thickness model illustrates that the substantial increase in ocean sediment thickness since 120 Ma reduces the modeled sea level drop from the ageing and deepening of the ocean basins during this time period by about 120 m (black versus light blue curve in Figure 12b), while the simplified global age-latitude-based sediment thickness relationship only reduces the sea level drop from deepening ocean basins since 120 Ma by about 40 m (black versus light red curve in Figure 12b). The equivalent reduction in sea level drop based on our modified implementation of Conrad's (2013) model is about 50 m (Figure 12b). Note that other factors, not considered here, also affect eustasy, including emplacement of large igneous provinces and the reduction in ocean floor area after Pangea breakup (Müller et al., 2008).

Our method also predicts sediment thickness in large unmapped regions of the present-day seafloor including South China Sea, Celebes Sea, Sulu Sea, northern Philippine Sea, the north Pacific off Kamchatka, and the Canada Basin (Figure 8). These regions are tectonically complex and not easily extrapolated using the present-day sediment thickness grid. As a proportion of deep-sea sediment contains carbonate, our predictive algorithm provides a framework for constraining the contribution of seafloor carbonates to the global carbon cycle over time.

6. Conclusions

In a novel application of pyGPlates (www.gplates.org) we have developed a method to compute the mean distance of any given parcel of ocean floor to the nearest passive continental margin at any given point

during its lifetime. Together with the age-area distributions of the ocean crust through time, this allows us to apply a regression algorithm that predicts sediment thicknesses and long-term decompacted sedimentation rates since 200 Ma, using third-order polynomial relationships. The distance to the nearest passive margin only affects sediment thickness substantially if it is smaller than about 2,000 km, allowing us to capture the difference in the sediment thickness-age relationship for oceans bounded by passive margins versus oceans largely surrounded by subduction zones. Our model quantifies and excludes the contribution of rivers which would effectively add the equivalent of a 31 m thick layer of sediment globally. Not considering river contributions in our model in this fashion would bias our predictions during times when these relatively young rivers did not exist—namely for our model of sedimentation during the Jurassic and Cretaceous periods when both highly elevated orogens and associated rivers were rare.

Our method is superior to manually separating the Pacific, Atlantic, and Indian oceans, or even more detailed oceanic regions, to compute separate sediment thickness-age relationships, as our method allows us to consider, in an automated fashion, the mean proximity of any given parcel of ocean floor to passive margins throughout its lifetime, capturing the history of now subducted ocean basins and complex regions even where the nature of plate boundaries has switched from active to passive and vice versa through time. Our method produces present-day sediment thickness and sedimentation rate maps that match observations better than other approaches, but most importantly is adaptive to changing ocean basin configurations and tectonic settings through time.

We show that the mean sediment thickness decreases from ~220 m at 200 Ma to a minimum of ~140 m at 130 Ma, reflecting the replacement of old, sediment-rich, Panthalassic ocean floor with young sediment-poor mid-ocean ridges, followed by an increase to ~365 m toward the present, reflecting the progressive growth of the global system of passive margins, along which ageing ocean floor gradually accumulated large thicknesses of terrigenous sediments. Mean long-term sedimentation rates increase from ~0.5 cm/ky at 160 Ma to over 0.8 cm/ky today, caused by enhanced terrigenous sediment influx along lengthened passive margins, superimposed by the onset of ocean-wide carbonate sedimentation. Our results suggest that the effect of sediments alone led to sea-level rise by about 130 m between 120 Ma and today, reflecting the substantial increase in modeled mean oceanic sediment thickness from about 150 m at 120 Ma to ~365 m at present-day. This effect counteracted the contemporaneous ageing and deepening of the ocean basins, alleviating the concomitant sea-level fall.

Our predictive algorithms coupled to a plate tectonic model provide an improved framework for constraining the seafloor sediment-driven eustatic sea-level component. The algorithms allow the computation of sediment thickness and sedimentation rate maps for any time in the geological past for which GPlates-compatible plate and passive continental margin reconstructions and oceanic paleo-age grids are available. This opens the opportunity to analyse the evolution of now completely destroyed pre-Pangea ocean basins in terms of their sediment budget, ultimately contributing to our understanding of ancient ocean carbon reservoirs and long-term climate. Future work may explore how to utilize the fundamental physics of sediment production and accumulation, including terrigenous and biogenic sedimentation. This would fully exploit paleogeographic and paleoclimate reconstructions and models to create dynamic maps of sedimentation through time, taking into consideration mountain building and climate change. Such models may better represent regions of anomalous high sedimentation rates which all current parameterized models fail to capture accurately, including major river discharge regions such as the Bengal Fan, localized regions of anomalously high deep sediment accumulation in subduction zones, fracture zone troughs, and graben structures.

Acknowledgments
This research was supported by the Australian Research Council (ARC) ITRP grant IH130200012. We thank David Kohn from the Sydney Informatics Hub and Sabin Zahirovic for technical help. We are grateful to William Hay for comments on an earlier version of the manuscript and to Laurent Husson for providing valuable feedback on our analysis and discussion of rivers. We thank Peter Olson, two anonymous reviewers, and Editor-in-Chief Thorsten Becker for detailed reviews that greatly improved the manuscript. All georeferenced figures were created using Generic Mapping Tools software. All gridded data and workflows are available for download at ftp://ftp.earthbyte.org/Data_Collections/Dutkiewicz_etal_2017_G3/.

References

Amante, C., & Eakins, B. W. (2009). *ETOPO1 1 arc-minute global relief model: Procedures, data sources and analysis* (NOAA Technical Memorandum NESDIS NGDC-24). Boulder, CO: National Geophysical Data Center, NOAA. https://doi.org/10.7289/V5C8276M

Bahr, D. B., Hutton, E. W., Syvitski, J. P., & Pratson, L. F. (2001). Exponential approximations to compacted sediment porosity profiles. *Computers & Geosciences*, *27*(6), 691–700. https://doi.org/10.1016/S0098-3004(00)00140-0

Berger, W. H., & Winterer, E. L. (1974). Plate stratigraphy and the fluctuating carbonate line. In K. J. Hsü & H. C. Jenkyns (Eds.), *Pelagic sediments: On land and under the sea* (pp. 11–48). Oxford, UK: Blackwell Publishing Ltd. https://doi.org/10.1002/9781444304855

Bishop, C. M. (2006). *Pattern recognition and machine learning* (738 p.). New York, NY: Springer.

Bornemann, A., Aschwer, U., & Mutterlose, J. (2003). The impact of calcareous nannofossils on the pelagic carbonate accumulation across the Jurassic-Cretaceous boundary. *Palaeogeography, Palaeoclimatology, Palaeoecology*, *199*(3), 187–228. https://doi.org/10.1016/S0031-0182(03)00507-8

Boss, S. K., & Wilkinson, B. H. (1991). Planktogenic/eustatic control on cratonic/oceanic carbonate accumulation. *The Journal of Geology*, *99*(4), 497–513. https://doi.org/10.1086/629513

Broecker, W. S., Klas, M., Clark, E., Bonani, G., Ivy, S., & Wolfli, W. (1991a). The influence of $CaCO_3$ dissolution on core top radiocarbon ages for deep-sea sediments. *Paleoceanography*, *6*, 593–608. https://doi.org/10.1029/91PA01768

Broecker, W. S., Klas, M., Clark, E., Bonani, G., Ivy, S., & Wolfli, W. (1991b). Sedimentation rates calculated on surface sediment samples from different site of the Atlantic and Pacific Oceans (Table 1). *PANGAEA*. https://doi.org/10.1594/PANGAEA.52464

Capone, D. G., & Hutchins, D. A. (2013). Microbial biogeochemistry of coastal upwelling regimes in a changing ocean. *Nature Geoscience*, *6*(9), 711–717. https://doi.org/10.1038/ngeo1916

Carter, L., Orpin, A. R., & Kuehl, S. A. (2010). From mountain source to ocean sink—The passage of sediment across an active margin, Waipaoa Sedimentary System, New Zealand. *Marine Geology*, *270*(1), 1–10. https://doi.org/10.1016/j.margeo.2009.12.010

Chase, Z., & Burckle, L. H. (2015). Compilation of ^{230}Th-normalized opal burial and opal concentrations from Southern Ocean surface sediments. *PANGAEA*. https://doi.org/10.1594/PANGAEA.846117

Chase, Z., Kohfeld, K. E., & Matsumoto, K. (2015). Controls on biogenic silica burial in the Southern Ocean. *Global Biogeochemical Cycles*, *29*(10), 1599–1616. https://doi.org/10.1002/2015GB005186

Clift, P. D. (2002). A brief history of the Indus River. *Geological Society Special Publications*, *195*(1), 237–258. https://doi.org/10.1144/GSL.SP.2002.195.01.13

Conrad, C. P. (2013). The solid Earth's influence on sea level. *Geological Society of America Bulletin*, *125*(7–8), 1027–1052. https://doi.org/10.1130/B30764.1

Curray, J. R. (2014). The Bengal depositional system: From rift to orogeny. *Marine Geology*, *352*, 59–69. https://doi.org/10.1016/j.margeo.2014.02.001

Cwienk, D. S. (1986). Recent and glacial age organic carbon and biogenic silica accumulation in marine sediments (Master's thesis, 272 p.). Narragansett, RI: University of Rhode Island.

Dijkstra, E. W. (1959). A note on two problems in connexion with graphs. *Numerische Mathematik*, *1*(1), 269–271

Divins, D. L. (2003). *Total sediment thickness of the World's oceans and marginal seas*. Boulder, CO: National Geophysical Data Center.

Figueiredo, J., Hoorn, C., Van der Ven, P., & Soares, E. (2009). Late Miocene onset of the Amazon River and the Amazon deep-sea fan: Evidence from the Foz do Amazonas Basin. *Geology*, *37*(7), 619–622. https://doi.org/10.1130/G25567A.1

Galloway, W. E., Whiteaker, T. L., & Ganey-Curry, P. (2011). History of Cenozoic North American drainage basin evolution, sediment yield, and accumulation in the Gulf of Mexico basin. *Geosphere*, *7*(4), 938–973. https://doi.org/10.1130/GES00647.1

Gibbons, A., Zahirovic, S., Müller, R., Whittaker, J., & Yatheesh, V. (2015). A tectonic model reconciling evidence for the collisions between India, Eurasia and intra-oceanic arcs of the central-eastern Tethys. *Gondwana Research*, *28*(2), 451–492. https://doi.org/doi.org/10.1016/j.gr.2015.01.001

Goudie, A. S. (2005). The drainage of Africa since the Cretaceous. *Geomorphology*, *67*(3), 437–456. https://doi.org/10.1016/j.geomorph.2004.11.008

Hamilton, E. L. (1976). Variations of density and porosity with depth in deep-sea sediments. *Journal of Sedimentary Research*, *46*(2), 280–300.

Hay, W. W., Rosol, M., Sloan, J., & Jory, D. (1988b). Plate tectonic control of global patterns of detrital and carbonate sedimentation. *Developments in Sedimentology*, *42*, 1–34. https://doi.org/10.1016/S0070-4571(08)70163-8

Hay, W. W., Sloan, J. L., & Wold, C. N. (1988a). Mass/age distribution and composition of sediments on the ocean floor and the global rate of sediment subduction. *Journal of Geophysical Research*, *93*(B12), 14933–14940. https://doi.org/10.1029/JB093iB12p14933

Hoorn, C., Guerrero, J., Sarmiento, G. A., & Lorente, M. A. (1995). Andean tectonics as a cause for changing drainage patterns in Miocene northern South America. *Geology*, *23*(3), 237–240. https://doi.org/10.1130/0091-7613(1995)023<0237:ATAACF>2.3.CO;2

Kohavi, R. (1995). *A study of cross-validation and bootstrap for accuracy estimation and model selection*. Paper presented at International joint conference on artificial intelligence. Stanford, CA: Morgan Kaufmann Publishers Inc.

Lyle, M. (2003). Neogene carbonate burial in the Pacific Ocean. *Paleoceanography*, *18*(3), 1059. https://doi.org/10.1029/2002PA000777

Lyle, M. W. (2015). Pacific Neogene carbonate accumulation rates. *PANGAEA*. https://doi.org/10.1594/PANGAEA.841501

Matthews, K. J., Maloney, K. T., Zahirovic, S., Williams, S. E., Seton, M., & Müller, R. D. (2016). Global plate boundary evolution and kinematics since the late Paleozoic. *Global and Planetary Change*, *146*, 226–250. https://doi.org/10.1016/j.gloplacha.2016.10.002

Miller, K. G., Kominz, M. A., Browning, J. V., Wright, J. D., Mountain, G. S., Katz, M. E.,. . . Pekar, S. F. (2005). The Phanerozoic record of global sea-level change. *Science*, *310*(5752), 1293–1298. https://doi.org/10.1126/science.1116412

Milliman, J. D., & Farnsworth, K. L. (2011). *River discharge to the coastal ocean: A global synthesis* (384 p.). Cambridge, UK: Cambridge University Press. https://doi.org/10.1017/CBO9780511781247

Milliman, J. D., & Syvitski, J. P. (1992). Geomorphic/tectonic control of sediment discharge to the ocean: The importance of small mountainous rivers. *The Journal of Geology*, *100*(5), 525–544. https://doi.org/10.1086/629606

Müller, R. D., Sdrolias, M., Gaina, C., Steinberger, B., & Heine, C. (2008). Long-term sea-level fluctuations driven by ocean basin dynamics. *Science*, *319*(5868), 1357–1362. https://doi.org/10.1126/science.1151540

Müller, R. D., Seton, M., Zahirovic, S., Williams, S. E., Matthews, K. J., Wright, N. M.,. . . Hosseinpour, M. (2016). Ocean basin evolution and global-scale plate reorganization events since Pangea breakup. *Annual Review of Earth and Planetary Sciences*, *44*, 107–138. https://doi.org/10.1146/annurev-earth-060115-012211

Olson, P., Reynolds, E., Hinnov, L., & Goswami, A. (2016). Variation of ocean sediment thickness with crustal age. *Geochemistry, Geophysics, Geosystems*, *17*, 1349–1369. https://doi.org/10.1002/2015GC006143

Potter, P. E. (1997). The Mesozoic and Cenozoic paleodrainage of South America: A natural history. *Journal of South American Earth Sciences*, *10*(5–6), 331–344. https://doi.org/10.1016/S0895-9811(97)00031-X

Powell, M. J. (1978). A fast algorithm for nonlinearly constrained optimization calculations. In G. A. Watson (Ed.), *Numerical analysis, Lecture notes in mathematics* (pp. 144–157). Berlin, Springer.

Raymo, M. (1994). The Himalayas, organic carbon burial, and climate in the Miocene. *Paleoceanography*, *9*(3), 399–404. https://doi.org/10.1029/94PA00289

Rea, D. K. (1994). The paleoclimatic record provided by eolian deposition in the deep sea: The geologic history of wind. *Reviews of Geophysics*, *32*(2), 159–195. https://doi.org/10.1029/93RG03257

Rea, D. K., Lyle, M. W., Liberty, L. M., Hovan, S. A., Bolyn, M. P., Gleason, J. D.,. . . Owen, R. M. (2006). Broad region of no sediment in the southwest Pacific Basin. *Geology*, *34*(10), 873–876. https://doi.org/10.1130/G22864.1

Rebesco, M., Hernández-Molina, F. J., Van Rooij, D., & Wåhlin, A. (2014). Contourites and associated sediments controlled by deep-water circulation processes: State-of-the-art and future considerations. *Marine Geology*, *352*, 111–154. https://doi.org/10.1016/j.margeo.2014.03.011

Robinson, S. A., Williams, T., & Bown, P. R. (2004). Fluctuations in biosiliceous production and the generation of Early Cretaceous oceanic anoxic events in the Pacific Ocean (Shatsky Rise, Ocean Drilling Program Leg 198). *Paleoceanography*, *19*(4), 1–19. https://doi.org/10.1029/2004PA001010

Rona, P. A., & Richardson, E. S. (1978). Early Cenozoic global plate reorganization. *Earth and Planetary Science Letters*, *40*(1), 1–11. https://doi.org/10.1016/0012-821X(78)90069-9

Sant, D., & Karanth, R. (1993). Drainage evolution of the lower Narmada valley, western India. *Geomorphology*, *8*(2–3), 221–244. https://doi.org/10.1016/0169-555X(93)90039-5

Seiter, K., Hensen, C., & Zabel, M. (2005a). Benthic carbon mineralization on a global scale. *Global Biogeochemical Cycles*, *19*, GB1010. https://doi.org/10.1029/2004GB002225

Seiter, K., Hensen, C., & Zabel, M. (2005b). Sedimentation rates of surface sediments: A compilation from different sources. *PANGAEA*. https://doi.org/10.1594/PANGAEA.227904

Southam, J. R., & Hay, W. W. (1977). Time scales and dynamic models of deep-sea sedimentation. *Journal of Geophysical Research*, *82*(27), 3825–3842. https://doi.org/10.1029/JC082i027p03825

Stankiewicz, J., & de Wit, M. J. (2006). A proposed drainage evolution model for Central Africa—Did the Congo flow east? *Journal of African Earth Sciences*, *44*(1), 75–84. https://doi.org/10.1016/j.jafrearsci.2005.11.008

Stein, C. A., & Stein, S. (1992). A model for the global variation in oceanic depth and heat flow with lithospheric age. *Nature*, *359*(6391), 123–129. https://doi.org/10.1038/359123a0

Sykes, T. J. (1996). A correction for sediment load upon the ocean floor: Uniform versus varying sediment density estimations—Implications for isostatic correction. *Marine Geology*, *133*(1), 35–49. https://doi.org/10.1016/0025-3227(96)00016-3

Tibshirani, R. (1996). Regression shrinkage and selection via the lasso. *Journal of the Royal Statistical Society, Series B*, *58*, 267–288. https://doi.org/10.1111/j.1467-9868.2011.00771.x

Whittaker, J. M., Goncharov, A., Williams, S. E., Müller, R. D., & Leitchenkov, G. (2013). Global sediment thickness data set updated for the Australian-Antarctic Southern Ocean. *Geochemistry, Geophysics, Geosystems*, *14*, 3297–3305. https://doi.org/10.1002/ggge.20181

Wobbe, F., Lindeque, A., & Gohl, K. (2014). Anomalous South Pacific lithosphere dynamics derived from new total sediment thickness estimates off the West Antarctic margin. *Global and Planetary Change*, *123*, 139–149. https://doi.org/j.gloplacha.2014.09.006

Geochemistry, Geophysics, Geosystems

Supporting Information for

Predicting sediment thickness on vanished ocean crust since 200 Ma

A. Dutkiewicz[1], R. D. Müller[1], X. Wang[2], S. O'Callaghan[2], J. Cannon[1] and Nicky Wright[1]

[1]EarthByte Group, School of Geosciences, University of Sydney, Sydney NSW 2006, Australia, [2]Data61, CSIRO, Australian Technology Park, Eveleigh, NSW 2015, Australia.

Contents of this file

Text S1
Figures S1 to S5

Introduction

This supporting information provides details on the construction of grids of mean distance to the nearest passive margin, grids of the age of oceanic crust, grids of predicted sediment thicknesses based on published relationships, and a plot of mean sediment thicknesses through time based on our model and previously published relationships.

Text S1. Mean distance to nearest passive margin calculation

Mean distance grids are calculated for geological times spanning 0–230 Ma in 1 My increments. At each geological time the ocean floor existing at that time is arranged into a regular grid of parcels (with continental regions masked out). For each parcel in the grid the mean distance to the nearest passive margin over that parcel's lifetime is calculated. To achieve this the position of a parcel is incrementally reconstructed back until that parcel's time of creation (at a mid-ocean ridge). At each time increment over this reconstruction period the minimum distance from the reconstructed parcel's position to the nearest reconstructed passive margin is calculated and finally these distances are averaged into a single mean distance for that parcel. This is repeated for all parcels in a grid and for all grids spanning 0–230 Ma to obtain 231 mean distance grids. These grids, along with age grids spanning 0–230 Ma, are used to generate the predicted sediment thickness and rate grids spanning 0–230 Ma.

Note that since the reconstruction model only goes back to 230 Ma there are some parcels of oceanic crust that cannot be reconstructed all the way back to their time of formation. At present-day this is not a problem since virtually all existing ocean floor was formed after 230 Ma and so we can track distances to passive margins over the entire lifetime of the present-day ocean floor. However, as we consider snapshots of the ocean floor existing at geological times further in the past we find progressively larger areas of old ocean crust that can only be reconstructed over part of its lifetime. In these cases, proximity contributions from passive margins around the time of formation of this ocean crust are progressively absent until, at 230 Ma, the mean distances of ocean floor consist of just a single snapshot (at 230Ma).

The minimum distance calculation involves finding the shortest path around all sediment transport obstacles. The path source is the reconstructed passive margins and the path destination is a reconstructed parcel of ocean floor. The obstacles include the continents (reconstructed boundaries between oceanic and continental crust) as well as mid-ocean ridge and subducting plate boundaries. We use a variant of Dijkstra's algorithm [*Dijkstra*, 1959] to progressively fill a uniform ocean floor grid with the shortest distance from reconstructed passive margins to each grid point. Essentially the algorithm starts at the reconstructed passive margins and spreads across the ocean grid in a circular wavefront pattern until all reachable grid points are filled with shortest path distances. To initialize the algorithm all grid nodes intersecting the reconstructed passive margins are assigned a distance of zero and added to the queue of nodes to visit. Each node in the queue is then visited in order of increasing distance to the passive margins so that closer nodes are visited first resulting in a circular wavefront visiting pattern. When a node is visited its distance is minimally propagated to its neighbouring nodes. Any neighbors updated with a smaller distance (than previously) are added to the queue to be visited. When there are no more nodes in the queue we have finished filling all nodes in the grid except those inside continents and those completely cut off from passive margins by mid-ocean ridge and subducting plate boundaries. Unreachable nodes are then assigned a large distance of approximately 20000 km (the great circle distance between two antipodal points on the globe) to ensure that time periods of “unreachable” passive margins for a given parcel of ocean floor are represented in a parcel's mean distance. The grid is then sampled at the reconstructed positions of the ocean floor parcels to find their shortest path distances to all passive margins. Note that the final mean distances are clamped to a maximum of 3000 km since larger distances have little effect on sedimentation (Fig. S1) and only tend to introduce noise in the predicted sediment thickness and rate grids.

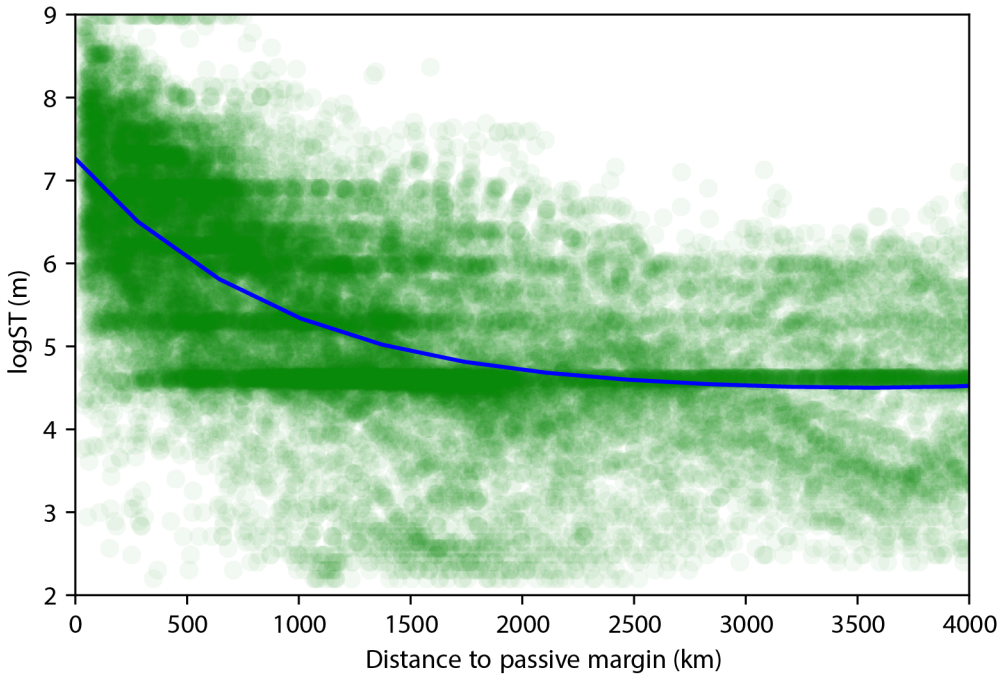

Figure S1. Scatter plot of distance to nearest passive margin versus a log of present-day sediment thickness with a line of best-fit (cubic polynomial) showing that sediment thickness decreases exponentially between a distance of 0 to 3000 km and remains almost constant between 3000 km and 4000 km.

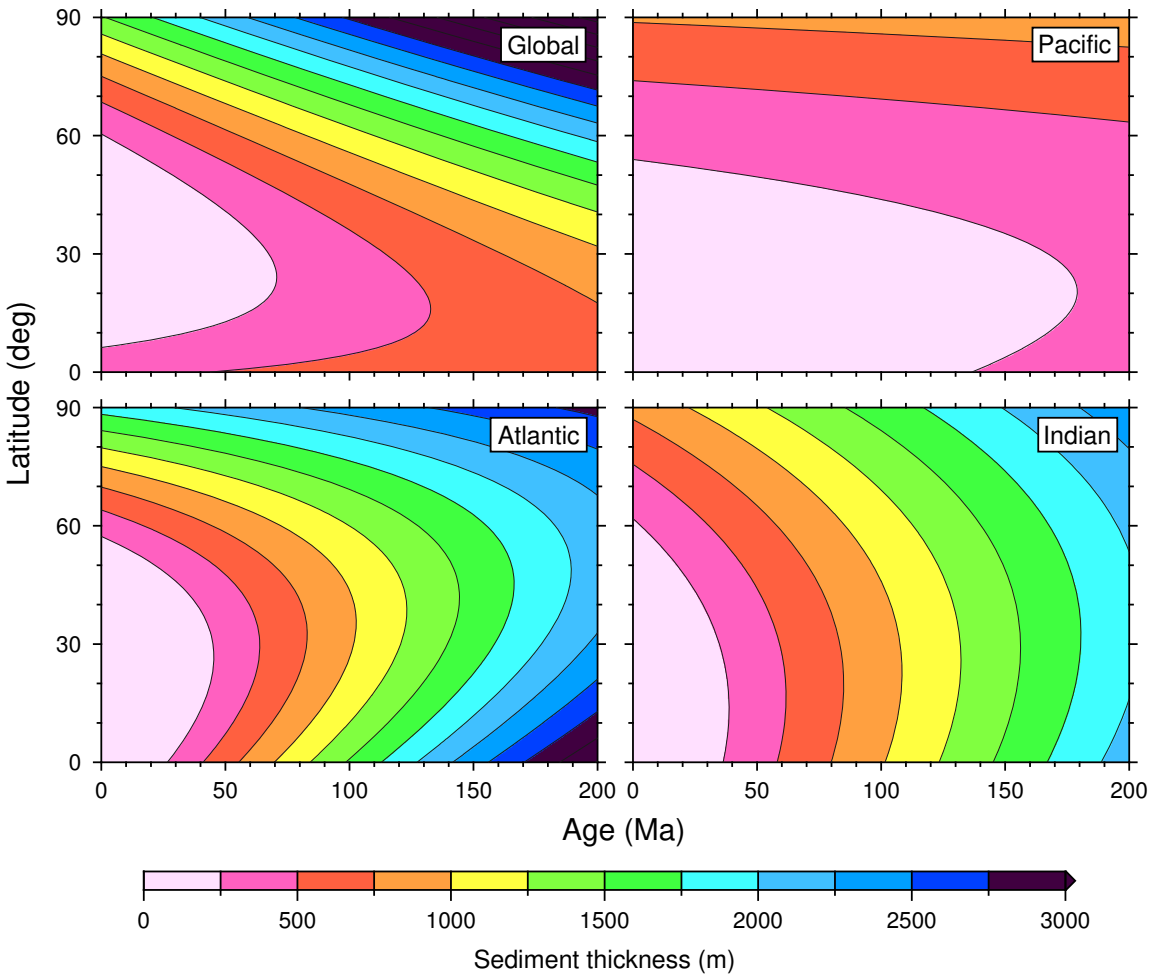

Figure S2. Global dependence of sediment thickness on oceanic crustal age and latitude from applying the method of Müller et al. (2008) to the present-day agegrid of Müller et al. (2016) (Global, upper left). The remaining panels illustrate regional relationships following the same method, but with sediment thickness data separated into the Pacific, Atlantic and Indian oceans.

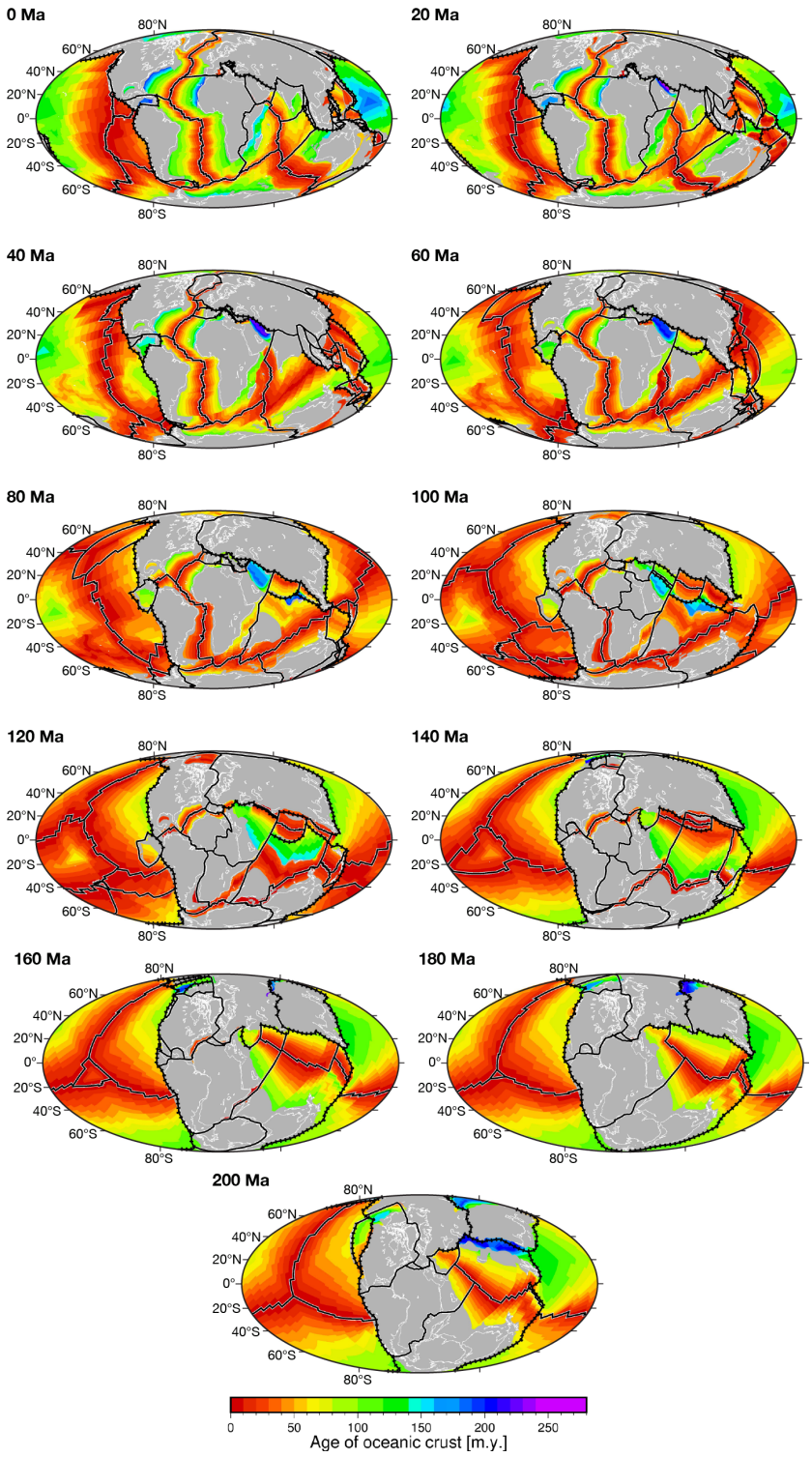

Figure S3. Global plate reconstructions from 200 Ma to the present day at 20 m.y. intervals, showing the age-area distribution of ocean crust at the time of formation from *Müller et al.* [2016]. Black hatched lines denote subduction zones, and black lines with white outlines denote plate boundaries. White outlines are paleo-coastlines and grey areas are continents. Mollweide projection.

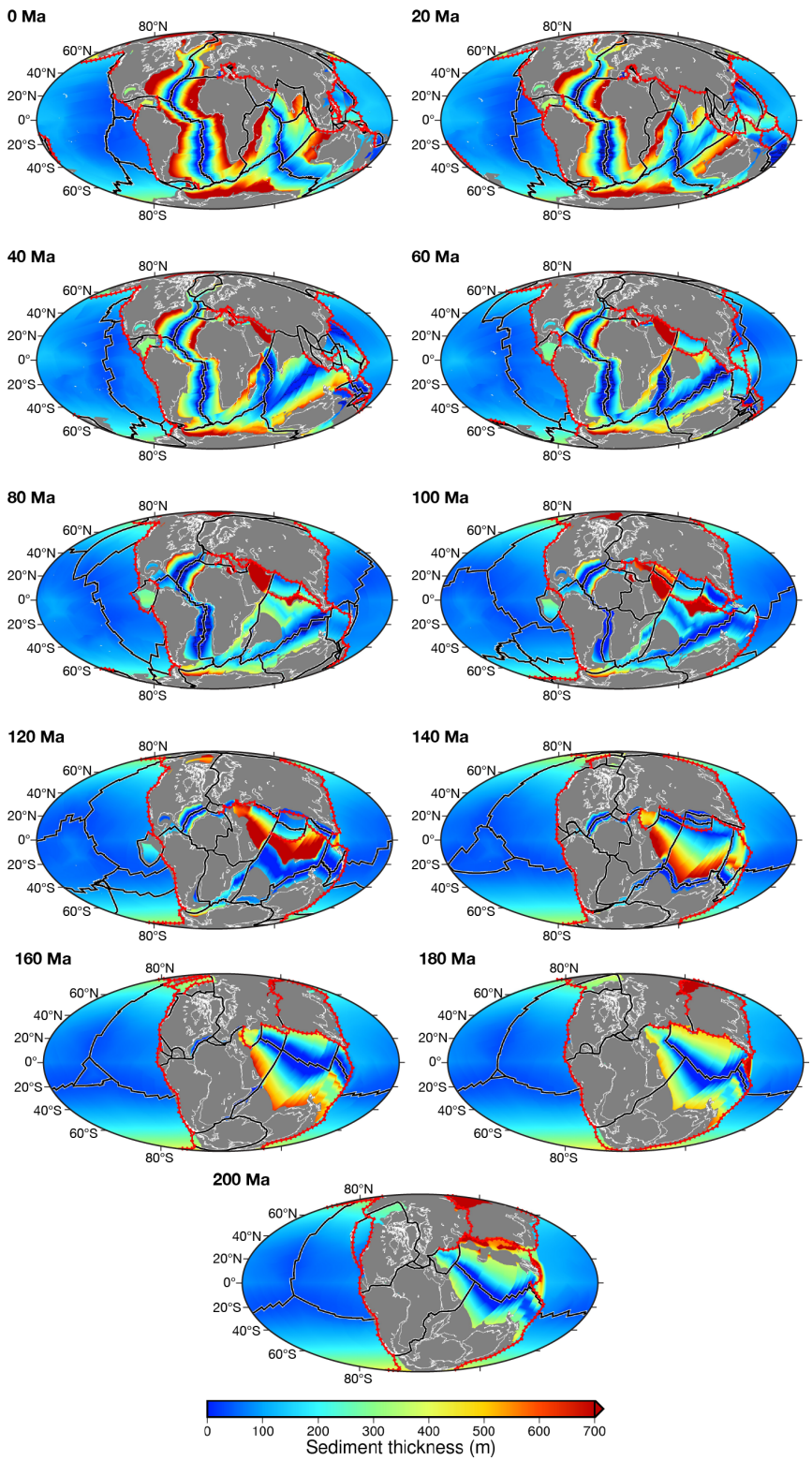

Figure S4. Predicted sediment thicknesses from 200 Ma to present day at 20 m.y. intervals based on the oceanic crustal age relationships determined for the Pacific, Atlantic and Indian ocean basins of *Conrad* [2013] that also consider the effect of latitude.

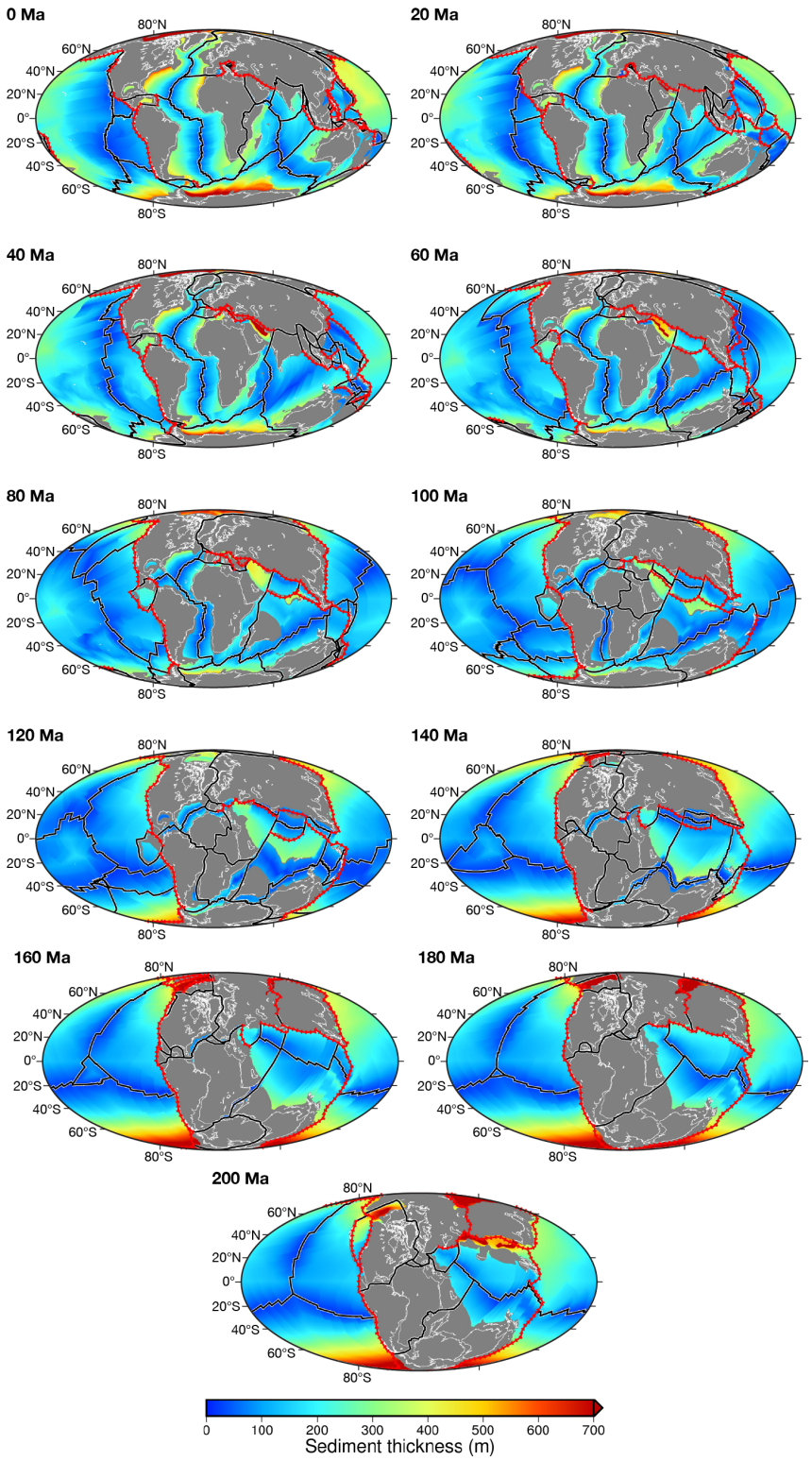

Figure S5. Predicted sediment thicknesses from 200 Ma to present day at 20 m.y. intervals based on the simplified relationship of sediment thickness as a function of oceanic crustal age and latitude from *Müller et al.* [2008], applied to the oceanic paleo-age grids of *Müller et al.* [2016].

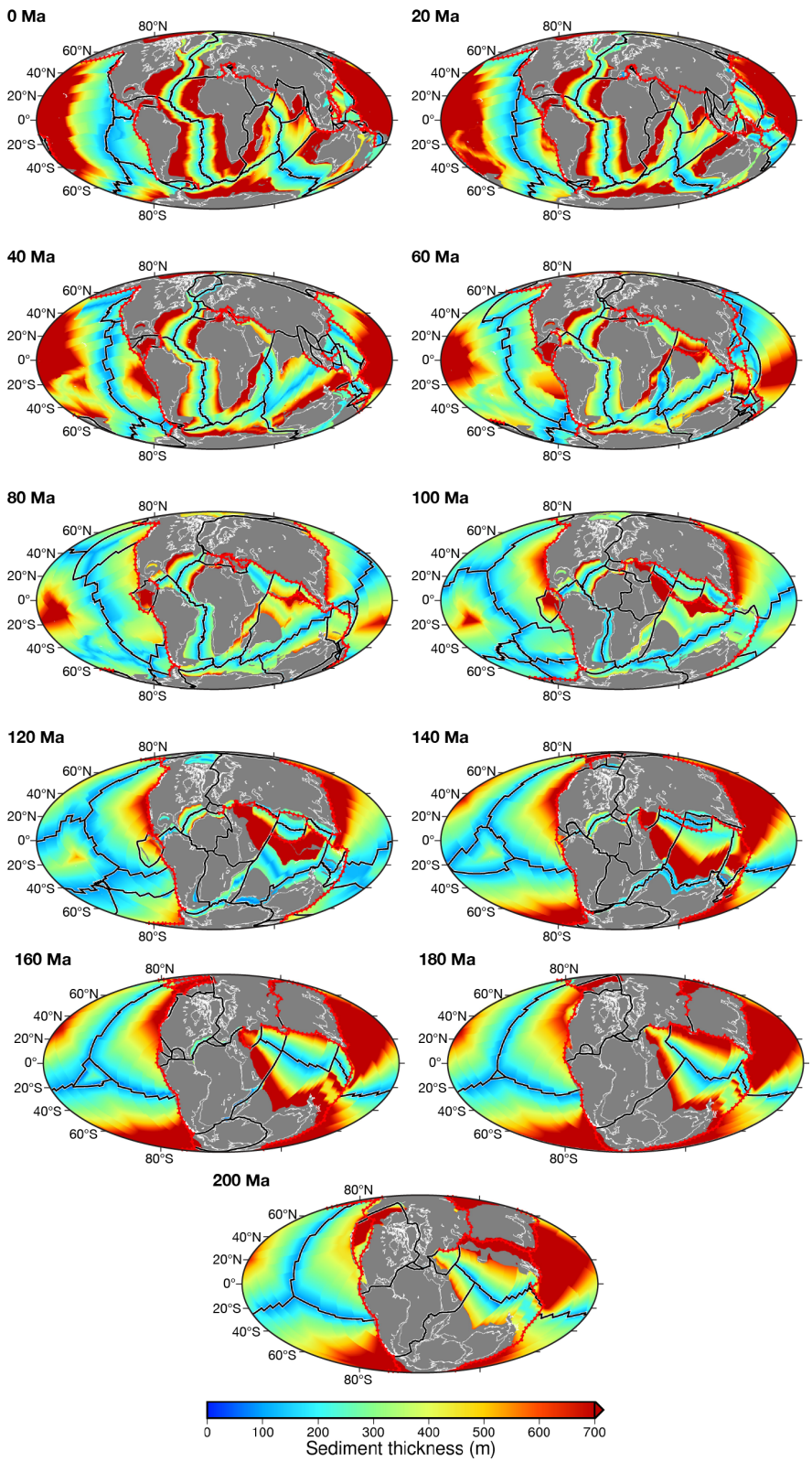

Figure S6. Predicted sediment thicknesses from 200 Ma to present day at 20 m.y. intervals based on the global best-fit cubic polynomial relationship of *Olson et al.* [2016]. Note the large overestimation of sediment thickness on old ocean crust, which reflects that *Olson et al.* [2016]

only used sediment thickness data on ocean crust aged 120 Ma and less, leaving their polynomial relationship ill-constrained for larger crustal ages.

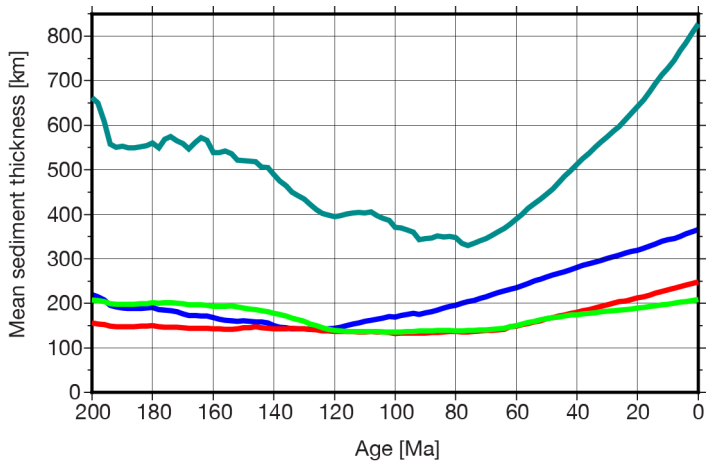

Figure S7. Mean sediment thickness through time. Blue curve is based on the oceanic crustal age-mean distance to nearest passive margin regression algorithm presented in this paper, red is based on the oceanic crustal age relationships determined for the Pacific, Atlantic and Indian ocean basins of *Conrad* [2013] that also consider a latitude dependence, green is based on the simplified relationship of sediment thickness as a function of oceanic crustal age and latitude from *Müller et al.* [2008], and dark cyan is based on the global best-fit polynomial relationship of *Olson et al.* [2016]. Note the large overestimation of sediment thickness based on *Olson et al.'s* [2016] relationship, reflecting their overestimation of sediment thickness on ocean crust older than 120 million years (see Fig. S6).

References

Conrad, C. P. (2013), The solid Earth's influence on sea level, *Geological Society of America Bulletin*, *125*(7-8), 1027-1052, doi: 10.1130/B30764.1

Dijkstra, E. W. (1959), A note on two problems in connexion with graphs, *Numerische Mathematik*, *1*(1), 269-271.

Müller, R. D., M. Sdrolias, C. Gaina, B. Steinberger, and C. Heine (2008), Long-term sea-level fluctuations driven by ocean basin dynamics, *Science*, *319*(5868), 1357-1362, doi: 10.1126/science.1151540.

Müller, R. D., M. Seton, S. Zahirovic, S. E. Williams, K. J. Matthews, N. M. Wright, G. E. Shephard, K. T. Maloney, N. Barnett-Moore, and M. Hosseinpour (2016), Ocean basin evolution and global-scale plate reorganization events since Pangea breakup, *Annual Review of Earth and Planetary Sciences*, *44*, 107-138, doi: 10.1146/annurev-earth-060115-012211.

Olson, P., E. Reynolds, L. Hinnov, and A. Goswami (2016), Variation of ocean sediment thickness with crustal age, *Geochemistry, Geophysics, Geosystems*, *17*(4), 1349-1369, doi: 10.1002/2015GC006143.